Southern California Permanent GPS Geodetic Array: Error analysis of daily position estimates and site velocities

Jie Zhang, Yehuda Bock, Hadley Johnson, Peng Fang, Simon Williams, Joachim Genrich, Shimon Wdowinski,[1] and Jeff Behr

Cecil H. and Ida M. Green Institute of Geophysics and Planetary Physics, Scripps Institution of Oceanography
La Jolla, California

Abstract. We analyze time series of daily positions estimated from data collected by 10 continuously monitoring Global Positioning System (GPS) sites in southern California during the 19-month period between the June 28, 1992 (M_W=7.3), Landers and January 17, 1994 (M_W=6.7), Northridge earthquakes. Each time series exhibits a linear tectonic signal and significant colored noise. Spectral power at frequencies in the range 5 yr^{-1} to 0.5 d^{-1} is dominated by white noise or possibly fractal white noise and is several orders of magnitude higher than what would be expected from random walk noise (in this short-period range) attributed by others to geodetic monument motions. Estimating a single slope for the time series' power spectra suggests fractal white noise processes with spectral indices of about 0.4. Site velocity uncertainties assuming this fractal white noise model are 2–4 times larger than uncertainties obtained assuming a purely white noise model. A combination white noise plus flicker noise (spectral index of 1) model also fits the data and suggests that the velocity uncertainties should be 3–6 times larger than for the white noise model. We cannot adequately distinguish between these two noise models, nor can we rule out the possibility of a random walk signal at the lowest frequencies; these questions await the analysis of longer time series. In any case, reducing the magnitude of low-frequency colored noise is critical and appears to be best accomplished by building sites with deeply anchored and braced monuments. Otherwise, rate uncertainties estimated from continuous GPS measurements may not be improved significantly compared to those estimated from infrequent campaign-mode measurements.

Introduction

Measurements of radio signals from the Global Positioning System (GPS) satellites have been used for more than 10 years to estimate crustal deformation. In the campaign GPS mode, a network of stations is measured periodically, typically once or twice a year over a time interval of several years. Station positions are estimated for each measurement period with respect to a consistent terrestrial reference frame. The precision of these estimates is often assessed by their repeatability defined by the weighted root-mean-square (RMS) scatter of individual coordinate components (i.e., north, east, and vertical) about a linear trend. Horizontal station velocities are then determined either by linear regression of individual coordinate components or by simultaneous estimation of positions and velocities. In estimating velocities, several assumptions are made which are predicated by the noncontinuous nature of the observations. First, the rate of change of position is linear in time, unless a site was subjected to significant coseismic/postseismic displacements [e.g., *Bock et al.*, 1993; *Genrich et al.*, 1996; *Savage and Svarc*, 1997]. Second, the position estimates are statistically uncorrelated. Third, it is assumed that the offset between the

antenna phase center and the geodetic mark (monument) is perfectly known for each measurement period. This is often difficult to achieve in practice since the GPS antenna is almost always recentered and releveled over the mark for each measurement period. These are precision operations prone to errors that are often compounded when different operators and/or hardware are used from one campaign to the next. Furthermore, site-specific errors such as multipath [e.g., *Counselman and Gourevitch*, 1981; *Georgiadou and Kleusberg*, 1988], signal scattering [*Elósegui et al.*, 1995; *Jaldehag et al.*, 1996], and antenna phase center variations [e.g., *Schupler et al.*, 1994] complicate this assumption. Finally, it is assumed that geodetic monuments are stable, i.e., they are firmly anchored to a subsurface layer that is representative of the Earth's crust.

How do these assumptions apply to continuous GPS measurements? Continuous GPS certainly minimizes antenna setup errors since the antennas are permanently attached to the Earth by some kind of monument, although replacements in hardware and firmware may sometimes occur over the lifetime of a project as improvements are made in GPS technology or when equipment malfunctions. Site-specific errors such as multipath, signal scattering, and antenna phase center variations are important but may not be as critical since repeated observation scenarios from day to day and averaging over a 24-hour observation window, typical for continuous GPS arrays, tend to reduce (but not eliminate) these problems [e.g., *Genrich and Bock*, 1992]. Experience with other types of continuous geodetic measurements indicates, however, that instability of geodetic monuments [e.g., *Karcz et al.*, 1976] introduces significant

---

[1]Now at Department of Geophysics and Planetary Sciences, Tel Aviv University, Ramat Aviv, Israel.

temporal correlations in the data. Expansive clays in near-surface rocks can cause monument motions comparable to the measurement precision of GPS, complicating the detection of tectonic phenomenon. For example, at the Ida and Cecil Green Piñon Flat Observatory (PFO), monument motions have been the largest source of noise for continuously recording strain meters and tiltmeters [Wyatt, 1982, 1989]. This is despite the stable geological setting, a thin (< 10 m) layer of decomposed granite overlying competent rock, with no alluvium, and despite the care taken to emplace them. Wyatt et al. [1982] reviewed the horizontal and vertical movements of these monuments, measured by optical anchors. Motions are dominated by long-period displacements of about 0.5 mm/yr, controlled primarily by weathering. Smaller elastic deformations caused by precipitation loading and tidal strains show the near surface to consist of weak material. Upon thorough wetting of the surface layers, mineral expansion lifts the surface by as much as 1 mm. During dessication, the ground subsides, ultimately below its original level. These vertical movements are accompanied by horizontal ones of the same magnitude [Wyatt, 1989].

The power spectrum for monument displacements shows the ground to undergo random-walk-like motion, b, with standard deviations growing in proportion to the square root of time, t, according to $b=(1/2P_0 t)^{1/2}$, with P_0 the effective diffusion constant. For even the best monumentation at PFO, emplaced in apparently solid granite, $P_0 = 2.1 \times 10^{-15}$ m^2 Hz, giving $b = 0.18$ mm in a year's time. In other terrain, benchmark instability is likely to be larger as indicated by frequent two color geodimeter (distance) measurements [Langbein et al., 1987; Langbein and Johnson, 1995]. Time series of these distance measurements exhibit power spectra that rise at low frequencies in proportion to f^{-2} which is characteristic of random walk or Wiener-Lévy processes. The random walk noise in these data ranges from 1.3 to 4.0 mm/yr$^{0.5}$ and is attributed to monument instability [Langbein et al., 1990; Langbein and Johnson, 1997].

Johnson and Agnew [1995] performed simulations with synthetic data to investigate the effect of random walk on the estimation of station velocities by continuous geodetic measurements. They conclude that to achieve better estimates of station velocity from continuous GPS measurements compared to campaign measurements, monument instability must be held to a small fraction of the measurement system precision. One option is to avoid geologically unsuitable locations, but that could well eliminate broad areas of tectonic interest, e.g., the southernmost section of the San Andreas fault which is overlain by thick sediments or the entire Los Angeles basin. The other is to develop ways in which ground monuments can be accurately referenced to depths at which weathering effects can be neglected [e.g., Wyatt et al., 1989]. The use of deeply (~10 m) anchored and braced monuments with isolation from the top 3–4 m has been shown to be effective in reducing monument motion [Langbein et al., 1995].

The most extensive time series analysis of (quasi) continuous GPS observations to date has been presented by King et al. [1995] for a single 8-km baseline spanning the Hayward fault in northern California for nearly a 3-year period from 1991 to 1994. They did not detect a random walk signal in the estimated power spectral density and autocorrelation functions of their single relative position ("baseline") time series, although they recognized its shortness compared to longer continuous geodetic time series may have made such a signal undetectable.

We analyze time series of daily position estimates for the 10 sites of the southern California Permanent GPS Geodetic Array

(PGGA) described by Bock et al. [this issue] for the period between the June 28, 1992 (Mw=7.3), Landers and January 17, 1994 (Mw=6.7), Northridge earthquakes (Figure 1). We exclude the three months of post-Landers data at stations PIN1, PIN2, and ROCH, which are shown by Wdowinski et al. [this issue] to have a clear nonlinear postseismic signature. The PGGA data allow us to better constrain the degree of temporal correlation in GPS position data on a site by site basis and to obtain more realistic estimates of velocities and their uncertainties at plate-boundary-width scales. As with the analysis by King et al. [1995], we are limited by the short duration of our time series. With 19 months of data we can only begin to explore their low-frequency character; more definitive results must rely on longer spans of data. Nevertheless, the diversity of the array during this time period allows us to evaluate several important factors in designing and constructing a continuous GPS network, including monument design and site selection.

Time Series Analysis

Weighted linear regression of daily GPS positions yields estimates of slope and abscissa intercept. For interseismic deformation, the estimation of slope is the important quantity; for coseismic deformation, estimation of abscissa intercept is the dominant parameter. In Appendix A we derive analytic expressions for weighted linear regression to better quantify the effective end-member stochastic models of white noise and random walk noise processes. In the case of uncorrelated errors, velocity uncertainty σ_r is proportional to the magnitude of white noise a_{WN}, and inversely proportional to the total observation interval T and the square root of the number of measurements N according to (see equations (A21) and (A23))

$$\left(\sigma_f\right)_{WN} = \frac{a_{WN}}{T} \sqrt{\frac{12(N-1)}{N^2 + N}} \simeq \frac{2\sqrt{3} a_{WN}}{N^{1/2} T} \quad N >> 2 \quad (1)$$

This is the basis for the familiar $N^{1/2}$ increase in accuracy sometimes assumed for continuous GPS measurements compared to less frequent field measurements. The magnitude of the white noise component is limited by the inherent GPS system measurement error which may be as small as 1 mm or less [Genrich and Bock, 1992].

In the case of random walk noise (RWN) (see equation A(30)),

$$\left(\sigma_f\right)_{RWN} = \frac{b_{RWN}}{T^{1/2}} \quad (2)$$

That is, velocity uncertainty is proportional to the magnitude of random walk noise b_2 and inversely proportional only to the square root of the total time span T. It is independent of the number of observations. The presence of random walk motion in continuous GPS measurements of magnitudes 1.3–4 mm/yr$^{0.5}$ seen in longer series of conventional geodetic measurements by Langbein and Johnson [1997] would significantly degrade site velocity uncertainties as can be seen by comparing (1) and (2). Therefore, for the proper interpretation of crustal deformation based on estimated site velocities, it is critical to analyze the stochastic properties of GPS position time series.

Many physical phenomena approximate a power law process $x(t)$ with power spectrum of the form

$$S_x(\omega) = S_0(\omega / \omega_0)^{-\kappa} \quad (3)$$

where ω is spatial or temporal frequency, S_0 and ω_0 are normalizing constants, and κ is the spectral index [Mandlebrot
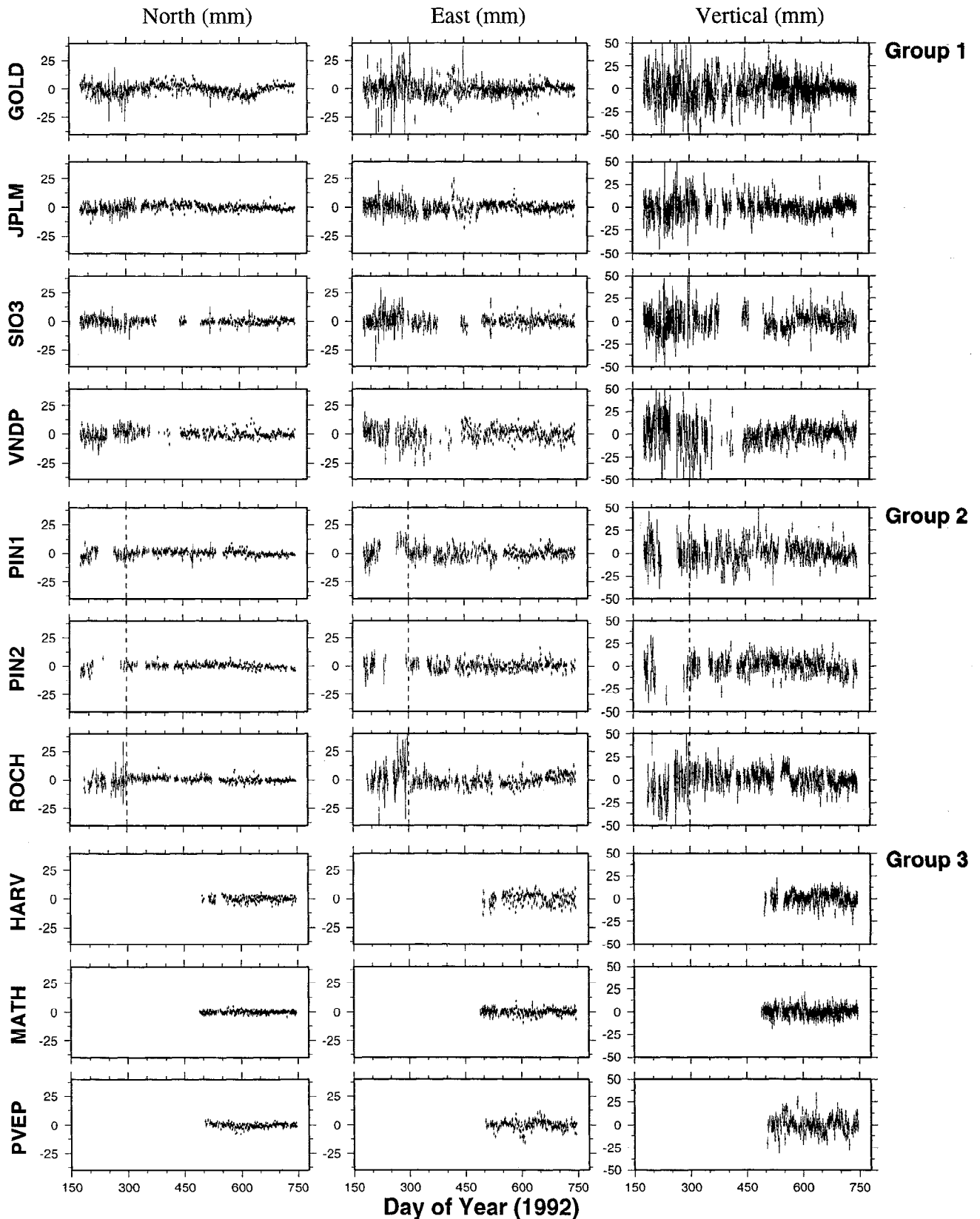
Figure 1. Demeaned and detrended filtered position time series for north, east, and vertical components of the 10 PGGA sites, divided into 3 groups. Group 1 has sites with full data spans between the Landers and Northridge earthquakes (567 days), only coseismically displaced by the Landers earthquake; group 2 has sites both coseismically and postseismically displaced; and group 3 has sites which began operations about 9 months before Northridge earthquake. Listed for each time series is the weighted RMS scatter. All data to the left of the vertical dashed lines for sites in group 2 (PIN1, PIN2, ROCH) have been omitted from the time series analysis as described in the text.

and Van Ness, 1968]. The larger κ is in (3), the smoother is the process and the more dominant are the lower frequencies. Geophysical phenomena often approximate processes with spectral index in the range $1< \kappa <3$ [e.g., *Agnew*, 1992; *Davis et al.*, 1994] and are termed "fractal random walk" [*Mandlebrot and Van Ness*, 1968]. For classical Brownian motion ("random walk"), $\kappa = 2$. An example of a fractal random walk process is "Kolmogorov turbulence" with $\kappa = 5/3$ [*Kolmogorov*, 1941]. Processes with spectral index larger than 1 are nonstationary. "Fractal white noise" is defined within the range $-1< \kappa <1$ [*Mandlebrot*, 1983]. These processes are stationary or independent of time. Classical white noise has a spectral index of 0 and flicker noise has a spectral index of 1. We will use the term "colored noise" to refer to all noise processes other than classical white noise.

In this section, we use three different approaches to analyze PGGA time series for temporal correlations. First, we compute autocorrelation functions, as employed by *King et al.* [1995] for continuous GPS data. Next, we use a new approach applied previously by *Johnson and Agnew* [1995] to synthetic data and which assesses continuous time series for integer-valued spectral indices, i.e., white noise, flicker noise, and classical random walk noise. In this approach, the total measurement error is modeled as a sum of white noise and colored noise (flicker noise or random walk noise) sequences. A maximum likelihood algorithm is used to estimate the magnitude of each type of error according to *Langbein and Johnson* [1997]. Finally, we also estimate the spectral index of each time series by a single linear regression of its power spectrum.

Weighted Autocorrelation Analysis

A visual examination of the PGGA time series (Figure 1) indicates that several series exhibit long-period temporal correlations, in particular, site GOLD in the north component and site PVEP in the east component. The error bars are larger in the early part of all the series (except for the third group which have shorter time series), and there are significant gaps in several of the series, particularly in the first half of the time period considered. Power spectrum algorithms generally require evenly spaced and equally weighted continuous data. We begin our analysis, therefore, in the time domain with computation of autocorrelation and cross-correlation functions [*Papoulis*, 1965] that are less restricted by these problems. The daily 1-σ (formal) error bars are used to compute weighted functions.

The first- and second-order moments of a stationary stochastic process $x(t)$ are, respectively, the mean

$$\eta = E\{x(t)\} \tag{4}$$

and autocorrelation

$$R_x(\tau) = E\{x(t)\, x(t + \tau)\} \tag{5}$$

with joint second moment or cross correlation

$$R_{xy}(\tau) = E\{x\, (t + \tau)\, y(t)\} \tag{6}$$

where E denotes expected value and τ denotes lag time. The normalized autocorrelation function (also called the autocovariance function) is defined by

$$\rho_x(\tau) = \frac{R_x(\tau)}{R_x(0)} \tag{7}$$

where

$$R_x(0) = E\{x^2(t)\} = \sigma_x^2 \tag{8}$$

is the variance. The normalized autocorrelation at zero lag is unity by definition. Likewise the cross-correlation function is defined by

$$\rho_{xy}(\tau) = \frac{E[x(t + \tau)\, y(t)]}{\sqrt{R_x(0)\, R_y(0)}} \tag{9}$$

For a white noise (WN) process $w(t)$

$$\eta = E\{w(t)\} = 0 \tag{10}$$

$$R_{WN}(\tau) = \begin{cases} \sigma_{WN}^2 & ; \tau = 0 \\ 0 & ; \tau > 0 \end{cases} \tag{11}$$

$$\rho_w(\tau) = \begin{cases} 1 & ; \tau = 0 \\ 0 & ; \tau > 0 \end{cases} \tag{12}$$

A random walk (RWN) process $r(t)$, also known as a Wiener-Lévy process or Brownian motion, is a nonstationary normal process whose statistics are uniquely defined [*Papoulis*, 1965] by its mean

$$\eta = E\{r(t)\} = 0 \tag{13}$$

and variance

$$R_{RWN}(0) = E\{r^2(t)\} = \sigma_{RWN}^2 = \gamma t \tag{14}$$

The associated autocorrelation function between epochs t_1 and t_2 is

$$R_{RWN}(t_2 - t_1) = \begin{cases} \gamma t_2 & ; t_1 \geq t_2 \\ \gamma t_1 & ; t_1 \leq t_2 \end{cases} \equiv \gamma \min(t_1, t_2) \tag{15}$$

and the (normal) probability density function is given by

$$f(r,t) = \frac{1}{\sqrt{2\pi\sigma_{RWN}^2}} \exp\left[-\frac{r^2}{2\sigma_{RWN}^2} \right] \tag{16}$$

The scale factor γ indicates the magnitude of the random walk process. A random walk process can be shown to be the cumulative sum of independent, stationary normal increments [*Papoulis*, 1965] or, equivalently, as the integral of white noise

$$r(t) = \int_0^t w(\tau)\, d\tau \tag{17}$$

such that the white noise process $w(t)$ has zero mean and a flat spectrum

$$S_{WN}(\omega) = \gamma \tag{18}$$

The power spectrum for the random walk process will rise at low frequencies in inverse proportion to the square of the frequency ω.

We estimate the weighted autocorrelation function for a time series of N points as follows:

1. Demean and detrend the time series $x(t)$ to obtain a new series $\tilde{x}(t)$.

2. Compute the weight coefficients

$$\alpha_{n,\tau} = \sqrt{\tilde{x}_n^2 \sigma_{n+\tau}^2 + \tilde{x}_{n+\tau}^2 \sigma_n^2} \tag{19}$$

where σ_n and $\sigma_{n+\tau}$ are the formal standard deviations for the nth and $(n+\tau)$th points in the series, respectively.

3. Compute the normalized coefficients

$$\bar{\alpha}_{n,\tau} = \frac{\alpha_{n,\tau}}{\sum_{n=1}^{N-1} \alpha_{n,\tau}} \tag{20}$$

4. Compute the estimated weighted autocorrelation function

$$\tilde{R}_x(\tau) = \sum_{n=1}^{N-1} (\tilde{x}_n \tilde{x}_{n+\tau})\, \alpha_{n,\tau} \tag{21}$$

5. Normalize the weighted autocorrelation function

$$\hat{\rho}_x(\tau) = \frac{\tilde{R}_x(\tau)}{\tilde{R}_x(0)} \quad;\quad \hat{\rho}_x(0) = 1 \tag{22}$$

The normalized weighted cross-correlation functions are determined in an analogous manner by the unbiased estimator

$$\hat{\rho}_{xy}(\tau) = \frac{\tilde{R}_{xy}(\tau)}{\sqrt{\tilde{R}_x(0)\,\tilde{R}_y(0)}} \tag{23}$$

For finite data sets, as τ increases, the overlap region decreases, so the estimates (22) and (23) become increasingly unreliable [e.g., *Priestley*, 1981].

We compute the weighted autocorrelation functions in north, east, and vertical components for the PGGA time series (Figure 2). Because of the estimation problems described by *Priestley* [1981] for large lag times, we follow the approach of *King et al.* [1995] and keep the lag time to less than $N/3$. We use $\tau < 150$ days for stations operational for the entire 19-month period (Figures 2a and 2b), and $\tau < 75$ days for stations operational for less than a year (Figure 2c). This shows an important limitation to autocorrelation analysis: we are most interested in the very long time lags (low frequencies), but the results in this range are not useful and are not represented in Figure 2.

Analysis With Integer Spectral Indices

We apply a maximum likelihood estimator (MLE) described by *Langbein and Johnson* [1997] to evaluate the time series for linear combinations of white noise ($\kappa=0$) and colored noise sequences with integer spectral indices ($\kappa=1$, $\kappa=2$). We evaluate three possible stochastic models: white noise (WN), a combination of white noise and flicker noise (WN+FN), and a combination of white noise and random walk noise (WN+RWN). Each individual noise process is represented by a single standard deviation of normally distributed random variables. The magnitudes of white noise and flicker noise have units of distance (millimeters); for random walk noise the units are in terms of the expected motion after 1 year (millimeters per square root year). When the MLE algorithm cannot separate the two error sources (because, for instance, the time series is too short or one of the error sources is considerably larger than the other), then it will return a zero estimate for (usually) the colored noise term. This should not be taken to mean necessarily that there is no colored noise but simply that the algorithm is not capable of distinguishing it.

A measured station coordinate component can be modeled by an initial value of the component x_0 (abscissa intercept) and velocity r (assuming a linear accumulation of deformation) such that

$$x(t_i) = x_0 + rt_i + \varepsilon_x(t) \tag{24}$$

or in matrix form

$$y(t) = Ax(t) + \varepsilon(t) \tag{25}$$

with

$$A = \begin{bmatrix} 1 & t_1 \\ 1 & t_2 \\ \vdots & \vdots \\ 1 & t_N \end{bmatrix} ;\ y = \begin{bmatrix} x_1 \\ x_2 \\ \vdots \\ x_N \end{bmatrix} ;\ x = \begin{bmatrix} x_0 \\ r \end{bmatrix} \tag{26}$$

We assume that the error term is a linear combination of a sequence of uncorrelated unit-variance random variables α and a colored noise sequence β such that

$$\varepsilon(t) = a\alpha(t) + b_\kappa \beta(t) \tag{27}$$

Coefficients a and b_κ are the magnitude of white noise and colored noise, respectively. The covariance matrix of $x(t)$ is given by

$$C_x(t) = E\{\varepsilon^T(t)\,\varepsilon(t)\} = a^2 I + b_\kappa^2 J_\kappa(t) \tag{28}$$

where I is the identity matrix and J_κ is the colored-noise covariance matrix. Matrices I and J_κ have dimension N, the number of points in the time series. The subscript κ denotes the spectral index of the colored noise (i.e., $\kappa = 1$ for flicker noise, $\kappa = 2$ for random walk noise). The covariance matrices for white noise, random walk noise, and flicker noise are given in Appendix B.

Using the MLE algorithm, we estimate coefficients a and b_κ such that

$$\hat{C}_x(t) = \hat{a}^2 I + \hat{b}_\kappa^2 J_\kappa(t) \tag{29}$$

We have modified this algorithm to estimate simultaneously the velocity r, intercept x_0, coefficients (a, b_κ), amplitude and phase of a yearly component signal, and an arbitrary number of offsets in the time series. However, because these time series are so short, we have chosen not to allow the MLE routines to fit for an annual signal. When we did allow this as a test, the low-frequency noise in several series was absorbed into the annual term and the power law component returned zero estimates. It is likely that there are annual signals in some of these series, but with at most 19 months of data, it is too much to ask of the MLE technique to fit for both this and the power law term. The algorithm also estimates uncertainties for each parameter and confidence intervals through use of the Fisher information matrix which is related to the curvature of the MLE function at its maximum.

For a well-designed geodetic monument and in the absence of other site-specific errors, we would hope that $b_\kappa/a \ll 1$; i.e., the daily positions are temporally uncorrelated. When $b_\kappa/a \approx 1$, temporal correlations may not be visually evident in the time series (especially for short series); they nevertheless can have a significant detrimental effect on the uncertainties of site velocities estimated from the position data [*Johnson and Agnew*, 1995]. As the colored noise component becomes more dominant ($b_\kappa/a \gg 1$), the improvement in accuracy expected from continuous position measurements compared to infrequent measurements decreases dramatically [*Johnson and Agnew*, 1995].

Maximum likelihood estimates of the coefficients (a and b_κ) for all 30 PGGA time series are presented in Table 1 for the WN, WN+FN, and WN+RWN models; the velocities r estimated simultaneously with the coefficients are given in Table 2 for the WN and WN+FN models only.

Analysis With Fractional Spectral Indices

Although sampled evenly, some of the PGGA time series suffer from significant data gaps and are therefore not strictly
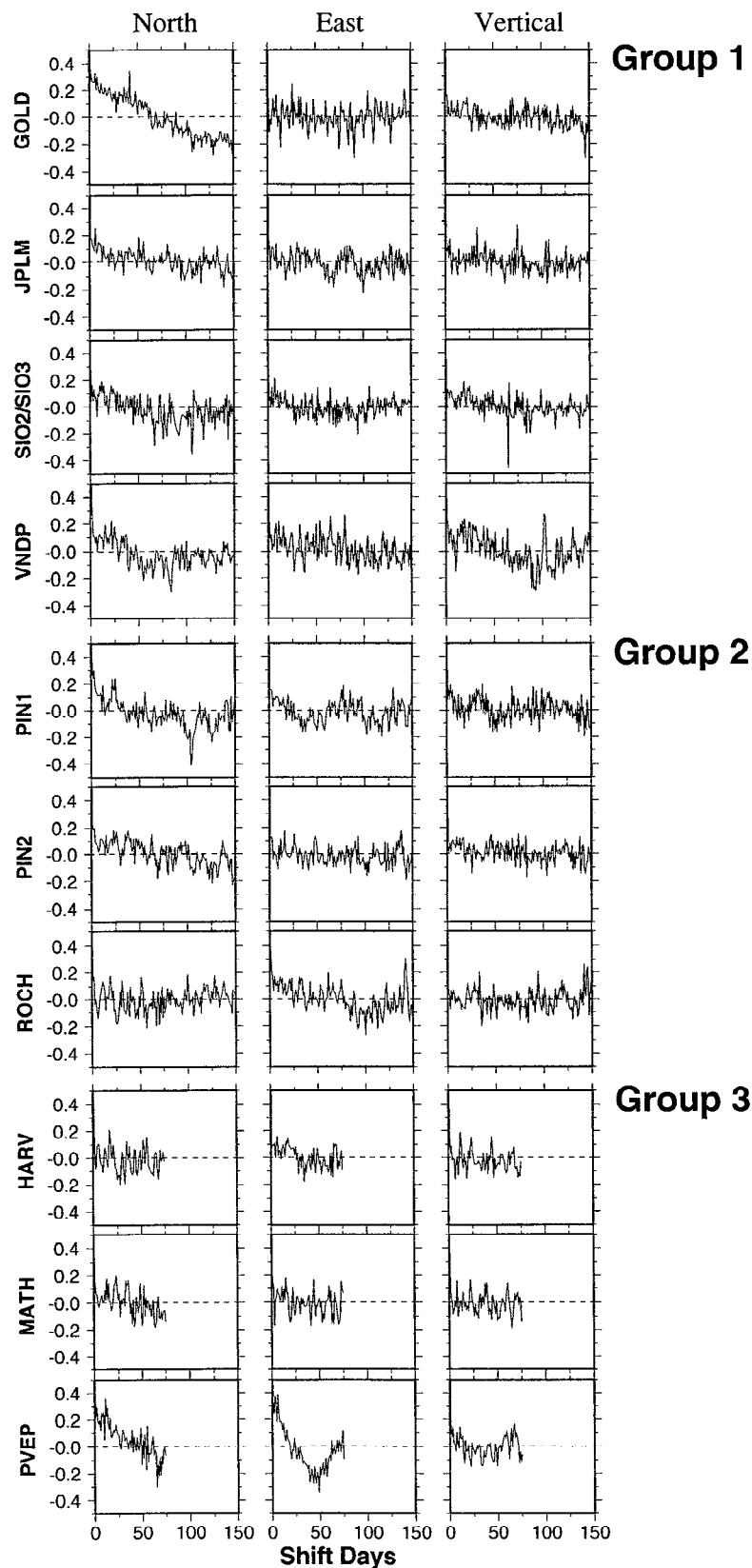
Figure 2. Weighted autocovariance functions of PGGA daily position time series (north, east, and vertical components) for the period between the Landers and Northridge earthquakes; the vertical scale denotes (unitless) covariances within the range [-0.5, 0.5] for a time lag up to 150 days (for groups 1 and 2), and up to 75 days for group 3. Grouping of sites is explained in Figure 1 caption.

Table 1. Results of Integer Spectral Index Analysis of Daily PGGA Position Time Series

Site Code	Monument Type	Site Changes	Component	WN+FN Model			WN+RWN Model			WN
				b_1 — FN, mm	a_1 — WN, mm	b_1/a_1	b_2 — RWN, mm/yr$^{0.5}$	a_2 — WN, mm	b_2/a_2, yr$^{-0.5}$	RMS, mm
Group 1										
GOLD	25 m tower	none	North	4.0±1.1	2.6±0.3	1.5	8.8±4.0	2.9±0.3	3.0	4.1
			East	4.0±2.4	5.8±0.6	0.7	7.7±6.3	6.0±0.5	1.3	6.3
			Vertical	9.5±5.2	10.3±1.4	0.9	16.9±16.3	11.0±1.1	1.5	11.7
JPLM	shallow concrete-based mobile VLBI monument	none	North	2.7±1.0	1.9±0.3	1.4	4.9±3.6	2.2±0.2	2.2	2.7
			East	4.5±1.9	3.3±0.6	1.4	11.8±9.5	3.7±0.4	3.2	4.2
			Vertical	6.7±3.5	6.7±1.0	1.0	10.6±10.8	7.3±0.8	1.5	7.9
SIO3	deeply anchored	hardware swap, SIO2 and SIO3 series combined	North	1.6±1.0	2.1±0.3	0.8	3.3±2.5	2.2±0.3	1.5	2.3
			East	3.1±1.8	3.7±0.5	0.8	6.0±4.7	3.8±0.5	1.6	4.1
			Vertical	8.1±3.5	7.0±1.1	1.2	17.7±10.5	7.5±0.8	2.4	8.6
VNDP	deeply anchored	hardware swap	North	3.7±1.7	2.6±0.5	1.4	4.9±4.2	3.0±0.4	1.6	3.3
			East	5.0±2.5	5.1±0.7	1.0	9.5±7.1	5.4±0.5	1.8	5.9
			Vertical	7.0±3.6	9.4±1.1	0.7	10.9±7.9	9.7±1.0	1.1	10.6
Group 2										
PIN1	deeply anchored	hardware swap	North	2.2±1.0	1.6±0.3	1.4	4.0±3.2	1.8±0.2	2.2	2.1
			East	3.1±2.0	3.6±0.5	0.9	7.5±6.5	3.8±0.5	2.0	4.0
			Vertical	6.5±4.4	8.1±1.2	0.8	10.7±13.4	8.6±1.0	1.2	9.1
PIN2	deeply anchored	no change	North	1.7±1.0	1.6±0.3	1.1	2.4±2.1	1.7±0.2	1.4	1.9
			East	2.0±2.2	3.4±0.5	0.6	*	3.6±0.4	*	3.6
			Vertical	4.2±3.0	6.8±0.9	0.6	6.4±6.3	7.0±0.8	0.9	7.4
ROCH	rod in massive rock outcropping	no change	North	1.4±1.2	1.7±0.3	0.8	*	1.9±0.2	*	1.9
			East	4.3±2.2	3.2±0.6	1.3	6.9±6.8	3.7±0.5	1.9	4.1
			Vertical	*	6.7±0.7	*	*	6.7±0.7	*	6.7
Group 3										
HARV	oil platform	no change	North	2.9±2.5	1.7±0.7	1.7	*	2.2±0.3	*	2.2
			East	3.2±2.4	4.3±0.7	0.7	7.3±7.1	4.4±0.6	1.7	4.7
			Vertical	4.9±6.4	5.5±1.5	0.9	*	6.1±0.8	*	6.1
MATH	rod in massive rock outcropping	no change	North	0.6±0.8	1.3±0.2	0.5	1.1±1.5	1.3±0.2	0.8	1.3
			East	1.6±1.6	2.4±0.4	0.7	3.1±4.6	2.5±0.3	1.2	2.6
			Vertical	2.7±4.0	4.3±0.8	0.6	*	4.6±0.5	*	4.6
PVEP	rod in massive concrete slab, atop missile silo	no change	North	1.7±0.9	1.6±0.3	1.1	3.6±2.8	1.7±0.3	2.1	2.0
			East	4.7±2.1	2.7±0.7	1.7	13.9±8.5	3.1±0.5	4.5	3.9
			Vertical	8.2±5.4	6.7±1.5	1.2	23.2±20.9	7.3±1.2	3.2	8.1

Stochastic models are white noise plus flicker noise (WN+FN) and white noise plus random walk noise (WN+RWN). White noise and colored noise coefficients and their ratios are estimated for each model. All uncertainties are 95% confidence intervals. The weighted root-mean-square (RMS) error (WN model) is provided for comparison. Group 1 has sites with full data spans, only coseismically displaced by the Landers earthquake; group 2 has sites both coseismically and postseismically displaced (the first 120 days of data are omitted from further analysis); and group 3 has sites which began operations about 9 months before the Northridge earthquake. For more information on monument type and site changes see Table 1 in *Bock et al.* [this issue].

*The maximum likelihood estimation algorithm failed to distinguish the colored noise coefficient.

Table 2. ITRF93 Velocity Estimates

Site Code	Component	WN	WN+FN	Ratio
Group 1				
GOLD	North	-6.2 ± 1.0	-5.8 ± 5.4	5.4
	East	-24.2 ± 1.5	-24.1 ± 5.6	3.7
	Vertical	2.1 ± 2.8	0.3 ± 13.0	4.6
JPLM	North	15.3 ± 0.6	15.6 ± 3.6	6.0
	East	-44.2 ± 1.0	-44.5 ± 6.1	6.1
	Vertical	6.2 ± 2.0	8.0 ± 8.6	4.3
SIO3	North	23.6 ± 0.6	23.6 ± 2.1	3.3
	East	-43.0 ± 1.1	-42.7 ± 4.0	3.6
	Vertical	13.5 ± 2.2	12.0 ± 10.1	4.6
VNDP	North	22.4 ± 0.9	22.7 ± 4.6	5.1
	East	-45.3 ± 1.6	-45.7 ± 6.6	4.1
	Vertical	-4.1 ± 2.7	-5.8 ± 9.4	3.5
Group 2				
PIN1	North	11.9 ± 0.8	12.6 ± 3.8	4.8
	East	-28.5 ± 1.5	-28.2 ± 5.5	3.7
	Vertical	7.0 ± 3.4	7.2 ± 11.5	3.4
PIN2	North	12.2 ± 0.8	12.0 ± 3.1	3.9
	East	-28.9 ± 1.6	-29.5 ± 4.1	2.6
	Vertical	4.5 ± 3.2	3.9 ± 8.5	2.7
ROCH	North	16.3 ± 0.7	16.3 ± 2.5	3.6
	East	-32.7 ± 1.6	-33.0 ± 7.3	4.6
	Vertical	0.9 ± 2.6	*	*
Group 3				
HARV	North	19.2 ± 2.0	19.6 ± 9.2	4.6
	East	-47.7 ± 4.3	-45.4 ± 11.3	2.6
	Vertical	-12.9 ± 5.6	-12.4 ± 16.8	3.0
MATH	North	18.1 ± 1.1	18.2 ± 2.3	2.1
	East	-39.1 ± 2.0	-39.3 ± 5.3	2.7
	Vertical	-3.7 ± 3.6	-3.2 ± 9.1	2.5
PVEP	North	24.7 ± 1.8	23.7 ± 5.7	3.2
	East	-57.8 ± 3.5	-58.3 ± 15.2	4.3
	Vertical	6.5 ± 7.3	10.7 ± 27.3	3.7

Velocity estimates in units of millimeters per year for white noise (WN), and white noise plus flicker noise (WN+FN) models. All uncertainties denote 95% confidence intervals. Ratio is WN+FN uncertainties divided by WN uncertainties. Site groupings are explained in Table 1.
*The maximum likelihood estimation algorithm failed to distinguish the flicker noise coefficient.

continuous. The requirement of evenly spaced, continuous data in power spectrum algorithms is primarily due to simplicity, computational efficiency, and a reliance on the fast Fourier transform. If one chooses to revert to the classical definition of the periodogram

$$P_x(\omega) = \frac{1}{N_0} \left| FT_x(\omega) \right|^2 \qquad (30)$$

where

$$FT_x(\omega) = \sum_{j=1}^{N_0} x(t_j) \exp(-i\omega t_j) \qquad (31)$$

for the data set

$$x(t_j); \; j=1,2,...,N_0$$

then the requirement for evenly spaced continuous data is removed. We evaluated the power spectrum of the time series using the redefined periodogram [Scargle, 1982]

$$P_x(\omega) = \frac{1}{2} \left\{ \frac{\left[\sum_j x_j \cos\omega(t_j-\tau) \right]^2}{\sum_j \cos^2\omega(t_j-\tau)} + \frac{\left[\sum_j x_j \sin\omega(t_j-\tau) \right]^2}{\sum_j \sin^2\omega(t_j-\tau)} \right\} \qquad (32)$$

where τ is defined by

$$\tan(2\omega\tau) = \frac{\sum_j \sin 2\omega t_j}{\sum_j \cos 2\omega t_j} \qquad (33)$$

Equation (32) reduces to (30) when the points are evenly spaced. The constant τ is an offset that makes the power spectrum independent of a constant time shift that may be applied to all $x(t_j)$ [Scargle, 1982]. This definition of a power spectrum is often referred to as an amplitude-squared spectrum and is different from the more typical power spectral density defined through the use of the Fourier transform.

Figure 3 shows the power spectra for the north, east, and vertical components of the time series on log-log plots. Also included are the theoretical spectra for the estimated WN+FN noise model from the MLE technique, a theoretical random walk spectrum with magnitude 1.5 mm/yr$^{0.5}$, and a single straight-line fit to the log-log values of each spectrum. The theoretical curves on these plots are in units of power spectral density. In order to compare these to the amplitude spectra of the time series, we have applied an approximate scaling factor to the amplitude spectra. Because the time series are nearly equally spaced in time, we believe this is good enough for a visual comparison. Assuming that a time series is dominated by a single power-law process (Equation (3)) then the spectral index κ can be estimated by fitting a straight line to the log-log values of the power spectrum. The spectral index is then the slope of that fit. Typically, the spectral index would be estimated by first finding the range of frequencies where the spectrum is well approximated by a single power law and then using an estimator to fit a straight line to the data within this range. This would remove the effect of the high-frequency end of the spectra where white noise (with a flat spectrum) may dominate and would be less sensitive to any outliers such as yearly, monthly, or daily peaks. However, owing to the relative shortness of the PGGA time series, we used a least squares fit to the whole power spectrum. Since the number of points in the power spectra increase toward the high-frequency end of the spectrum, a robust estimator would treat the low-frequency data (where the power law process is likely to dominate) as leverage points and apply less weight to them. This would result in a lower estimate for κ for a "red" spectra. The (nonrobust) least squares estimator will place more weight on the lower frequencies and will be more affected by possible seasonal peaks such as the obvious annual cycles in the GOLD north and PVEP east components, resulting in a larger estimate for κ. Overall, for the present time series, we feel that the least squares estimator is more appropriate than a robust estimator. The spectral index and its 95% confidence interval are plotted in the top right hand corner of each plot in Figure 3.

Precision of Site Position Estimates

We now apply autocorrelation, integer spectral index, and fractional spectral index analyses to evaluate the stochastic properties of the PGGA time series and, thereby, the precision of site position estimates. This is critical for extracting meaningful
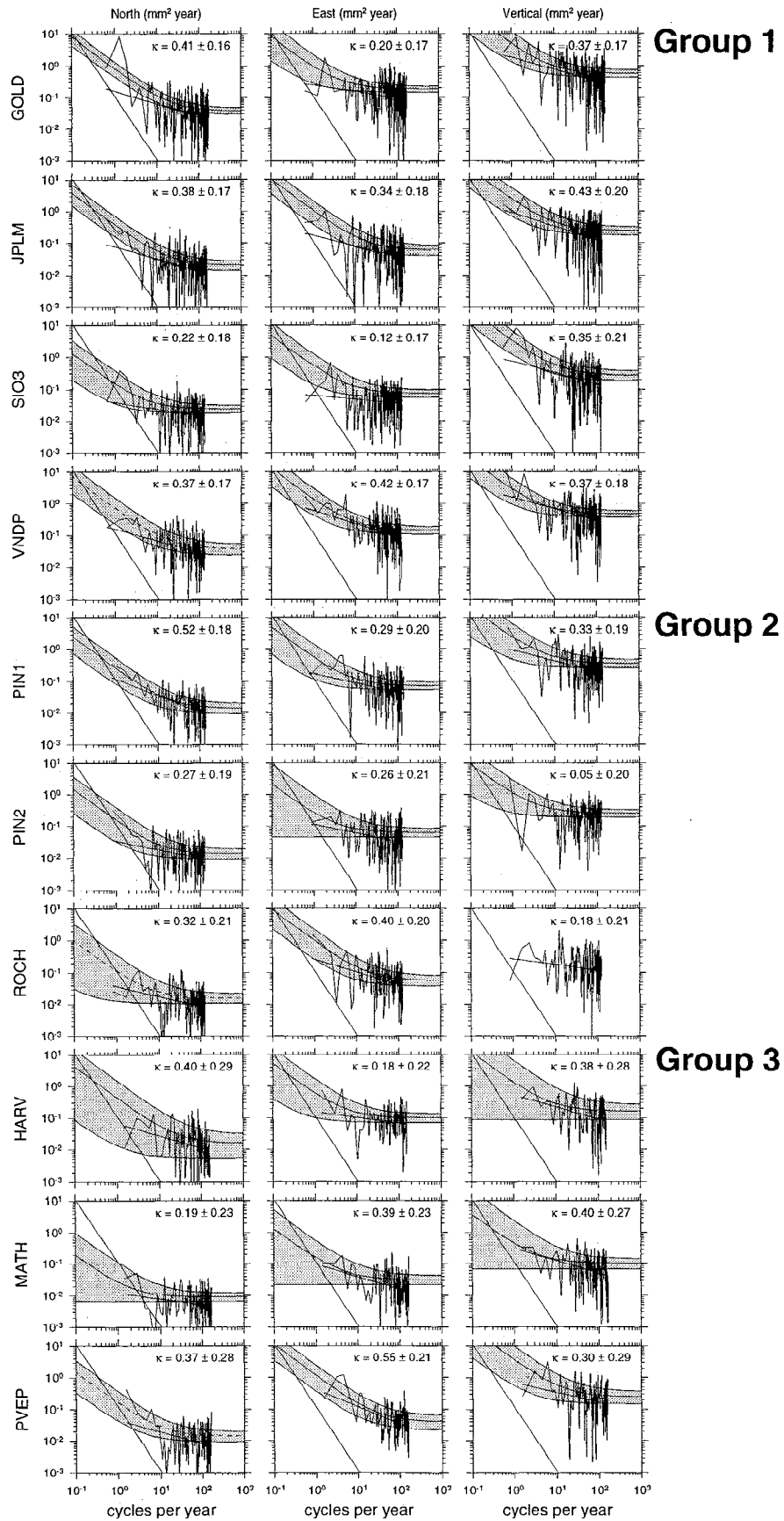
Figure 3. Fractional spectral analysis of the PGGA time series by site and coordinate component. Vertical axes have units of square millimeter years. Shown is each plot are (1) the amplitude spectrum (irregular line), (2) the least squares linear fit to the spectrum (solid straight line), (3) the estimated white noise plus flicker noise spectrum (dashed line) and its uncertainty band (shaded region), and (4) the random walk spectrum with magnitude 1.5 mm/yr$^{0.5}$ (dotted line). The least squares estimate of the spectral index κ and its uncertainty (95% confidence interval) are shown in the top right corner of each panel.

observations of tectonic processes including coseismic and postseismic deformation [*Wdowinski et al.*, this issue], and interseismic deformation [*Bock et al.*, this issue].

Autocorrelation Analysis

A visual examination of the autocorrelation functions suggests the presence of significant correlations in the north component of GOLD (Figure 2a) and north and east components of PVEP (Figure 2c). GOLD's north autocorrelation function exhibits positive correlation for very short lag times and negative correlation for longer lag times. PVEP exhibits temporal correlation in both horizontal components; the north autocorrelation decays linearly; the east component autocorrelation decays with negative slope for $\tau < 50$ days and then increases with positive slope. GOLD sits atop a 25 m steel tower while PVEP is situated in soft rock and clay on a coastal terrace [*Bock et al.*, this issue]. Autocorrelations of sites HARV, JPLM, MATH, PIN2, and ROCH exhibit no apparent temporal correlations or perhaps marginal correlations (JPLM north, PIN2 north, and ROCH east). The sites with antenna changes (PIN1 and VNDP) and eccentricities (SIO3) exhibit subtle correlations which may be artifacts of these changes.

If we ended our analysis at this point, we would arrive at the same basic conclusion as *King et al.* [1995] for their more limited data set, that there are no significant temporal correlations in the continuous GPS time series, except in our case for sites GOLD and PVEP. The weighted autocorrelation analysis tends to support the view that the PGGA time series are primarily white noise processes. Autocorrelation function analyses are not well suited, however, to characterization of nonstationary random processes [*Davis et al.*, 1994]. Therefore, if the PGGA time series are nonstationary random walk processes, for example, autocorrelation functions would not necessarily determine this. *King et al.* [1995] indicated that the rapid decay in the autocorrelation function for their continuous GPS data may have been just an artifact of the shortness of their time series.

Integer Spectral Index Analysis

The integer spectral index analysis of the PGGA time series (Table 1) indicates that (1) the white noise components are well determined in all cases and are statistically equivalent for the three models; (2) the magnitudes of the WN coefficients are independent of the length of the corresponding time series and are about 10–20% lower than the weighted RMS statistic; (3) the magnitudes of WN coefficients are about 2–4 mm in the north component, 4–5 mm in the east component, and 5–10 mm in the vertical component; (4) the FN coefficients b_1 are reasonably well determined, although their uncertainties are about 4 times larger than those for the WN coefficients; the algorithm fails to return a scaling coefficient for the vertical component of ROCH; and (5) the RWN coefficients b_2 are less well determined, with their uncertainties about the same order of magnitude as the estimates themselves; the algorithm fails to return a scaling coefficient for 6 of the time series. The failure of the algorithm to return scaling coefficients is the result of the shortness of the series; the relative magnitudes of the white and colored noise terms also play an important role.

We test whether either or both of the colored noise models, WN+FN and WN+RWN, fit the data better than the WN model. To do this we use the maximum log-likelihood-ratio test statistic [*Kendall and Stuart*, 1979]

$$\Lambda = \frac{\text{max likelihood 1}}{\text{max likelihood 2}}$$

$$= \exp[(\text{max–log–likelihood 1}) - (\text{max–log–likelihood 2})] \quad (34)$$

The test statistic Λ and the maximum value of the log-likelihood function for each model are given in Table 3 for both colored noise models. We consider that model 1 (WN) best fits the time series to be the null hypothesis and wish to test whether this hypothesis can be rejected in favor of the alternative hypothesis that model 2 (a colored noise model) better fits the data. To determine the probability distribution of Λ under the null hypothesis, we simulated 100 time series for each PGGA component given the model parameters for the WN model and then fit both this model and the colored noise models to the synthetic data and tabulated all 100 values of Λ. In all cases, the values of Λ were equal to 1.0 implying that the log-likelihood values under both the null and alternative hypotheses are identical. This means that the MLE routines do not fit the synthetic data any better when the possibility of colored noise is added to the null hypothesis model of WN. In other words, the routines are not "fooled" into finding colored noise if none is present. This is a very desirable property of the MLE technique and means that the likelihood ratio test statistic is a powerful test in rejecting this null hypothesis. We see in Table 3 that in all of the determinate cases, the colored noise models provide a clearly better fit than the WN model. From this we infer that the probability of the null hypothesis (WN) being correct is essentially zero, and we can reject it in favor of either of the colored noise models: thus the MLE technique shows that a white noise error model is not appropriate for the PGGA time series.

The maximum log-likelihood values for the WN+FN model are larger in most cases than those for the WN+RWN model but only by a small amount. To compare these two models against one another, we take the null hypothesis to be the WN+RWN model and the alternative hypothesis to be the WN+FN model. Unfortunately, the PGGA time series between the Landers and the Northridge earthquakes are not long enough to make such a test useful. We do note, however, that the 95% confidence intervals for the WN+RWN parameter estimates are often as large as the values themselves, while the WN+FN estimates are better determined. Further insight into the appropriate model will have to await the analysis of longer time series.

Fractional Spectral Index Analysis

Fractional spectral analysis of the time series is summarized in Figure 3. Shown in each panel are the power spectrum, the least squares estimate of the spectral index κ (again, assuming only a single straight-line fit) and its 95% confidence interval. The spectra show only a small tendency toward low values of κ by the high-frequency end of the spectrum, but at the same time we reiterate that the relatively short length of the time series certainly undersamples the lower frequencies.

In all cases, the spectral indices lie within the range [0.05, 0.55], although most values are well approximated by 0.4 ± 0.2 (95% confidence level). The uncertainties are about 0.10 for the longer series (Figures 3a and 3b), and 0.14 for the shorter series (Figure 3c). For each station, they generally agree within one-sigma for all three components. These observations suggest that the dominant colored noise contribution for all stations can be well described by a power law spectrum with spectral index of about $\kappa=0.4$. The associated variance of the process after time T is given by [*Agnew*, 1992]

$$\sigma^2_{\text{FWN}}(T) \propto T^{-0.6} \quad (35)$$

i.e., a decay for longer lag times. Whether this trend holds for all

Table 3. Log-Likelihood Tests for Stochastic Models

| Site Code | Component | Log-Likelihood | | | A-statistic | |
		WN	WN+FN	WN+RWN	WN+FN Versus WN	WN+RWN Versus WN
Group 1						
GOLD	North	2191.70	2333.00	2340.10	0.00	0.00
	East	1969.20	1976.20	1974.10	0.00	0.01
	Vertical	1554.30	1565.60	1562.40	0.00	0.00
JPLM	North	2207.50	2265.40	2260.70	0.00	0.00
	East	1939.30	1964.60	1958.80	0.00	0.00
	Vertical	1496.30	1514.70	1511.30	0.00	0.00
SIO3	North	1733.50	1740.10	1738.90	0.00	0.00
	East	1484.20	1492.00	1492.80	0.00	0.00
	Vertical	1212.40	1233.60	1234.80	0.00	0.00
VNDP	North	1775.30	1796.80	1791.10	0.00	0.00
	East	1468.80	1482.40	1483.90	0.00	0.00
	Vertical	1272.10	1290.60	1294.90	0.00	0.00
Group 2						
PIN1	North	1609.60	1636.20	1632.60	0.00	0.00
	East	1387.70	1393.50	1392.20	0.00	0.01
	Vertical	1113.30	1121.40	1120.50	0.00	0.00
PIN2	North	1502.50	1518.40	1517.50	0.00	0.00
	East	1303.30	1303.70	*	0.67	
	Vertical	1080.70	1086.70	1088.10	0.00	0.00
ROCH	North	1478.90	1480.50	*	0.20	*
	East	1232.40	1253.90	1050.90	0.00	0.00
	Vertical	1090.30	*	*	*	*
Group 3						
HARV	North	997.59	1000.40	*	0.01	*
	East	823.55	827.23	828.52	0.00	0.01
	Vertical	776.76	777.46	*	0.50	*
MATH	North	1232.90	1233.50	1233.90	0.55	0.37
	East	1068.10	1069.70	1068.80	0.20	0.50
	Vertical	931.78	932.14	*	0.70	*
PVEP	North	1035.50	1052.40	1054.60	0.00	0.00
	East	888.53	910.28	909.42	0.00	0.00
	Vertical	720.96	725.83	724.38	0.01	0.00

Models are white noise (WN), white noise plus flicker noise (WN+FN), and white noise plus random walk noise (WN+RWN). The larger the value, the more significant is the model. If the Λ-statistic is close to unity, the null hypothesis (WN) is accepted, otherwise it is rejected in favor of a colored noise model. Site groupings are explained in Table 1.

*The maximum likelihood estimation algorithm failed to distinguish the colored noise coefficient.

large lag times (and therefore renders the process stationary) cannot be determined from finite representations. Fortunately, for time series derived from GPS or other types of geodetic measurements, we are mostly concerned about the quantity and quality of noise within the time span of actual or potential measurements, i.e., seconds to decades. The issue of whether the observed noise is stationary is therefore mostly of theoretical interest. In the context of crustal deformation measurements we are more concerned with accessing the precision of quantities (i.e., site velocities) derived from our continuously sampled data. Specifically, for these time intervals, we want to determine the magnitude and character of time-correlated noise in relation to the end-member models of WN and RWN. For this purpose we have included in Figure 3 power spectral densities of the best fitting WN+FN model (see Table 1 for a_1 and b_1 values) and a RWN model with a scaling coefficient of $b_2 = 1.5$ mm/yr$^{0.5}$. On the basis of earlier referenced work [e.g., Langbein and Johnson, 1997], we can regard this random walk process as a representation of the level of site instability of a well-anchored monument.

An inspection of the spectra yields three important observations: (1) spectral power at higher frequencies is (not surprisingly) several orders of magnitude higher than what can be expected from monument instability; (2) spectral power for the east and vertical components is consistently higher than corresponding north component values; and (3) both the WN+FN model and a fractal white noise (FWN) of spectral index about 0.4 fit the observations in the available frequency range. These observations suggest that the power spectra at higher frequencies (5 yr^{-1} to 0.5 d^{-1}) are dominated by white noise and possibly a weakly time-correlated noise not related to monument instability. As possible sources for the observed correlated noise, we can safely disregard receiver noise as a major contributor, since it is much lower in magnitude and likely uncorrelated over the time intervals considered [e.g., Genrich and Bock, 1992]. Noise sources that are common to all sites (orbit errors, reference system orientation) have been essentially eliminated by filtering out a common-mode bias from the time series [Bock et al., this issue]. Not accounted for, however, are site-specific errors correlated with site-to-satellite observation geometry, including satellite sky coverage and track orientation. Contributors include multipath, antenna phase center variations, and possibly signal scattering. Satellite track orientation is the reason for different spectral power levels among the three components. The elevated

noise levels for the east and vertical components demonstrate (as was observed by other investigators earlier [e.g., *Dong and Bock*, 1989] that these components are more affected by the constellation geometry. Since day-to-day satellite constellations are essentially identical at a time lag of 4 min and repeat once per year (assuming no repositioning, major orbital changes, or activation/deactivation of satellites), we expect noise from these sources to be correlated for considerable periods. The generally good agreement in the spectral index between all three components is consistent with a common time-dependent source. Another explanation for the correlated noise is related to atmospheric effects. Although beyond the scope of this paper, we note that analysis of time series of hourly atmospheric zenith delay estimates (not position estimates) from 30 southern California continuous GPS sites show similar low-frequency characteristics in their power spectra for all sites.

If we extrapolate our observed power spectra to lower frequencies, we can compute cross-over frequencies where the measurement noise equals noise due to potential monument instability. For random walk monument noise with $b_2 = 1.5$ mm/yr$^{0.5}$ reported in other geodetic time series by *Langbein and Johnson* [1997] these corner frequencies are about 1.0 ± 0.5 yr^{-1} for the horizontal, and 0.3 ± 0.2 yr^{-1} for the vertical component (see *Langbein and Johnson* [1997], p. 602). To detect the presence of a corner frequency at f_0 using spectral techniques requires time series at least $5/f_0$ in length, or about 5 and 17 years for the values just given. If the PGGA time series do indeed exhibit RWN of this magnitude, tectonic velocity resolution would be controlled by monument instability rather than GPS-specific measurement noise for observation spans beyond something like 0.5 years. However, as indicated, we are unable to detect significant random walk noise in any of the PGGA time series because of the shortness of the time series and the magnitude of the white noise component. It will take considerably longer time series to better assess the colored noise characteristics of the PGGA data.

Measurement of Interseismic Deformation

Interseismic deformation is inferred from site velocities estimated by weighted linear regression (1-D) or simultaneous adjustment (2-D or 3-D) of repeated GPS position measurements. Site velocity estimation with WN and RWN models was compared earlier by deriving analytic expressions (equations (1) and (2)) which highlighted significant differences in velocity uncertainties achievable within the range of these two end-member processes. In light of the outcomes of the time series analyses of the PGGA data, we are now ready to estimate velocities and their uncertainties for each coordinate component. We then compare velocity uncertainties obtainable for several observation scenarios ranging from typical annual campaign surveys to continuous GPS measurements. Finally, we provide some suggestions for GPS site design.

Estimation of Site Velocities

Velocity estimates for each of the PGGA time series are given in Table 2 for the WN and WN+FN models, with respect to the International Terrestrial Reference Frame 1993 (ITRF93 [*Boucher et al.*, 1994]), as described by *Bock et al.* [this issue]. An important observation is that the velocity estimates themselves are not significantly affected by the assumed measurement model. For the WN model, velocity uncertainties are about 1–2 mm/yr horizontally and 3 mm/yr vertically, at the

95% confidence level, for the seven sites operational over the entire 19-month period, and about 2 times poorer for sites that became operational about a year after the Landers earthquake (Table 2). These uncertainties are consistent with equation (1) for equally spaced continuous data. That is, under the white noise assumption, velocity uncertainty is inversely proportional to the total time interval and the square root of the number of continuous measurements. We have demonstrated, however, that the WN model poorly fits the data and that there is significant colored noise in the time series which can be modeled either as fractal white noise (FWN) or white noise plus flicker noise (FN+WN).

There is no simple analytical expression (as for WN and RWN, equations (1) and (2)) nor at least a known covariance matrix (as for FN, equation (B3)) for estimating velocity uncertainties under the FWN model. However, it is still possible to get an approximate value for them. Part of the definition of a continuous fractional Brownian process is that the increments $\Delta x(t) = x(t + 1) - x(t)$ have a Gaussian distribution (with a standard deviation of $\sigma_{\Delta x}$ and zero mean, see also equations (11)–(15)). The same definition can be generalized to FWN processes. Over the range $0 \le \kappa < 3$, given the same $\sigma_{\Delta x}$, the value for σ_f^2 should be the same when the number of points in the time series is just two. For the case of WN, $\sigma_{\Delta x} = a\sqrt{2}$, and for RWN, $\sigma_{\Delta x} = b\sqrt{\Delta T}$. The uncertainty $\sigma_{\Delta x}$ can therefore be estimated either from the time series directly or from the WN+RWN estimates (Table 1). From simulated time series at a given κ, we find a relatively simple relationship between σ_f^2 and $\sigma_{\Delta x}$,

$$\sigma_f^2 \approx \frac{2^{3-\kappa} \sigma_{\Delta x}^2}{N^{3-\kappa} \Delta T^2} \qquad (36)$$

In Table 4 we show the appropriate scaling coefficients to be applied to the white noise velocity uncertainties to properly account for FWN, WN+FN, and WN+RWN, assuming that the series are continuous (i.e., that there are no data gaps). Velocity uncertainties for the WN+FN model are about 3–6 times larger than the uncertainties from the WN model (see Figure 4); for FWN the uncertainties are about 2–4 times larger.

A powerful internal test of the estimated site velocities (Table 2) is provided by nearby sites PIN1 and PIN2 which are about 50 m apart; both are constructed with deeply anchored monuments. According to both WN and WN+FN models, their velocities are statistically equivalent (at the 95% confidence level) and agree to about 0.5 mm/yr in the north component, 1.3 mm/yr in the east component, and 3.3 mm/yr in the vertical component. To rule out possible correlations between the position series for PIN1 and PIN2, Figure 5 shows the cross-correlation functions between their corresponding component time series. There appear to be only marginally significant cross correlations (although this does not completely rule them out). The baseline time series between PIN1 and PIN2 (PIN1-PIN2) shown in Figure 6 is impervious to any possible biases introduced by our regional filtering algorithm [*Wdowinski et al.*, this issue]. In the baseline representation, the WN model indicates zero relative horizontal velocity: -0.3± 0.7 mm/yr in the north, 0.4±1.0 mm/yr in the east, and a vertical velocity of -1.2 ± 2.8 mm/yr (all uncertainties are 95%). This is very consistent with the differenced individual site velocity estimates (Table 2) in horizontal components but less so for the vertical component. There is a small improvement in the white noise coefficient (a) in the baseline representation which is not surprising considering that most error sources are common-mode due to the close proximity of these two sites.

Table 4. White Noise Uncertainty Scale Factors

Site Code	Component	Uncertainty, mm/yr WN	Uncertainty, mm/yr FWN	Scale Factor FN	Scale Factor RWN
Group 1					
GOLD	North	1.0	2.3	5.1	18.4
	East	1.5	1.9	3.4	10.5
	Vertical	2.8	2.9	4.3	12.4
JPLM	North	0.6	2.4	5.2	15.6
	East	1.0	2.4	5.6	24.1
	Vertical	2.0	3.3	4.5	11.5
SIO3	North	0.6	2.0	3.7	12.3
	East	1.1	1.5	4.0	12.6
	Vertical	2.2	2.5	4.9	17.7
VNDP	North	0.9	2.6	5.8	12.8
	East	1.6	3.3	4.5	13.8
	Vertical	2.7	2.9	3.5	8.9
Group 2					
PIN1	North	0.8	3.8	5.5	16.4
	East	1.5	2.4	4.1	16.1
	Vertical	3.4	2.6	3.8	10.1
PIN2	North	0.8	2.1	4.7	10.9
	East	1.6	2.3	3.0	*
	Vertical	3.2	1.2	3.1	7.5
ROCH	North	0.7	2.5	3.9	*
	East	1.6	2.8	5.4	14.3
	Vertical	2.6	1.9	*	*
Group 3					
HARV	North	2.0	2.3	4.6	*
	East	4.3	1.6	2.5	5.9
	Vertical	5.6	2.6	2.9	*
MATH	North	1.1	1.8	1.9	3.4
	East	2.0	2.7	2.3	4.7
	Vertical	3.6	2.9	2.2	*
PVEP	North	1.8	2.2	3.0	3.6
	East	3.5	3.0	4.1	4.6
	Vertical	7.3	2.0	3.5	4.4
	Mean:	2.4 ± 0.6		4.0 ± 1.1	11.4 ± 5.3

Scale factors to be applied to white noise (WN) uncertainties (95% confidence) to take into account fractal white noise (FWN), flicker noise (FN), and random walk noise (RWN), assuming equally spaced, continuous time series. Site groupings are explained in Table 1.

*The maximum likelihood estimation algorithm failed to distinguish the colored noise coefficient.

Another comparison is an external one. The velocities (Table 5 and Figure 7) of all sites are computed with respect to the NUVEL1-A Pacific plate pole of rotation [*DeMets et al.*, 1990, 1994] after transformation of the ITRF93 velocities to the NNR NUVEL1-A reference frame [*Argus et al.*, 1991] using the rotation angles of *Boucher et al.* [1994]. In Figure 4a we plot the velocities of the PGGA sites with their 95% confidence ellipses for the WN and WN+FN models; in Figure 4b we plot the ellipses for the WN and FWN models. We have neglected the cross correlations between the north and east components which we know to be less than 0.1 from a preliminary simultaneous adjustment of positions and velocities of the PGGA sites (this is also indicated by their weighted cross-correlation functions). The velocity of VNDP agrees with the one estimated by *Feigl et al.* [1993] from an independent set of GPS and VLBI measurements collected over nearly a decade prior to the Landers earthquake, which indicates that the velocity of VNDP is within 1–2 mm/yr of NUVEL-1A Pacific plate motion. This site is sufficiently distant from the Landers earthquake epicenter so that its rate of deformation is not expected to have been affected [*Bock et al.*, this issue].

Neither of these comparisons can validate or invalidate any of the possible colored noise models. Table 4 summarizes the

velocity uncertainties for the components of the PGGA data under all four models investigated. There is clearly some amount of correlated data in these time series; the difficult part is constraining both the amount of this correlated noise and its spectral index. We have presented evidence earlier which leads us to reject the WN model and prefer the WN+FN model over the WN+RW model. We are left with two possible models, WN+FN and FWN, and we have no adequate statistical test by which to make a choice between the two. Visually comparing the amplitude spectra of the data in Figure 3 with the corresponding spectral shapes for the WN+FN and FWN models is also inconclusive. We thus have no way to choose between these last two noise models. Therefore we present our final estimates for the PGGA site velocities for both the FWN and WN+FN models, with respect to the NUVEL-1A Pacific plate pole of rotation (Table 5). The FWN velocity estimates are the same as the WN estimates, but the WN uncertainties are inflated (see equation (36)) according to the FWN spectral indices given in Table 4.

In Figure 7 we plot velocity uncertainties (1σ) for 0.5 to 10 years of continuous GPS measurements for the WN, WN+FN, and WN+RWN models. The corresponding scaling coefficients are averages of the horizontal component scaling coefficients listed in Table 4. Although these coefficients are obtained from
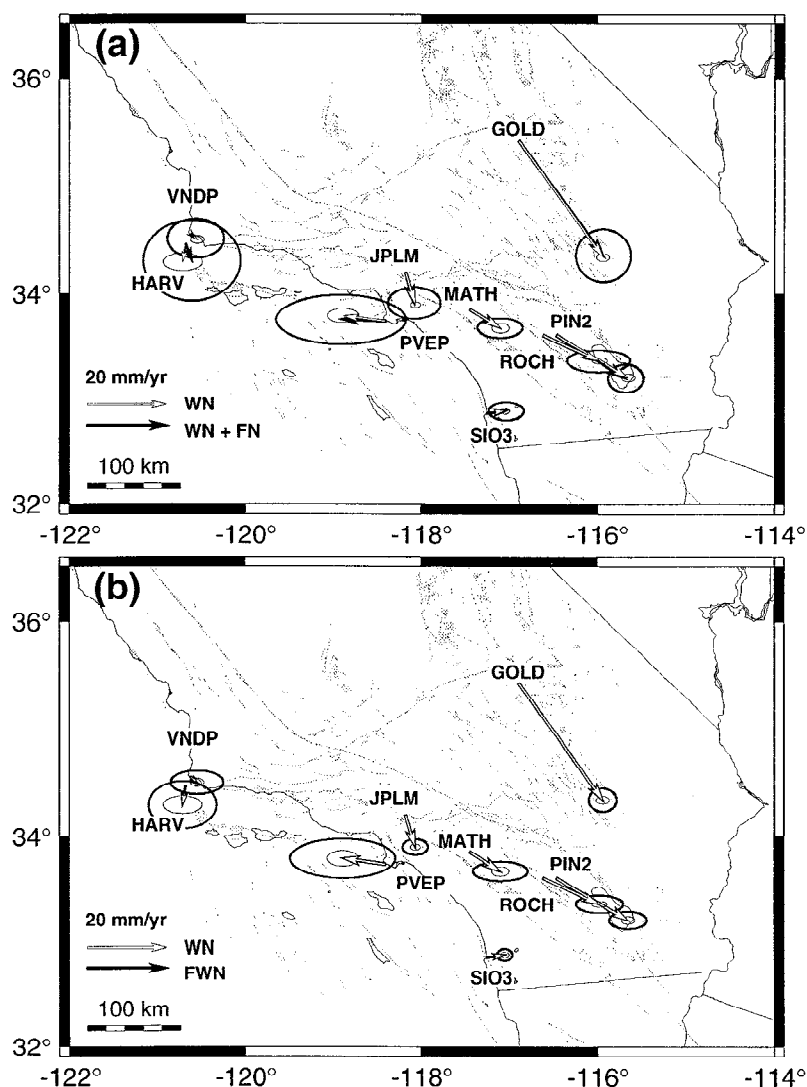
Figure 4. Observed horizontal site velocities relative to the Pacific plate estimated from the PGGA data. The velocities are estimated in the global ITRF93 reference frame, transformed to the NNR NUVEL-1A frame using the known small rotations between ITRF93 and NNR NUVEL-1A [*Boucher et al.*, 1994], and transferred to a fixed Pacific plate frame according to NUVEL-1A. Shown in both panels are 95% confidence ellipses. (a) The light arrows and thin ellipses are for the white noise (WN) model; the dark arrows and thick ellipses are for the white noise plus flicker noise (WN+FN) model. (b) The light arrows and thin ellipses are for a WN model; the dark arrows and thick ellipses are for the fractal white noise (FWN) model (see Table 4 for the scale factors applied for each model).

less than 2 years of actual (PGGA) measurements, the figure may provide a reasonable indication of what can be expected for site velocity uncertainties obtainable from longer spans of continuous GPS data under the three integer spectral index models.

Continuous Versus Campaign GPS

It is sometimes assumed that continuous GPS will provide much more precise velocity estimates than campaign GPS measurements over the same total time span, or equivalently that continuous GPS will achieve a desired velocity uncertainty much faster than infrequent campaign measurements. These assumptions are based on incomplete knowledge concerning the error characteristics of GPS position estimates, which can best be assessed by analysis of continuous time series. In light of the results of our time series analysis of only 19 months of PGGA data, we extrapolate to several 5-year measurement scenarios.

Whether our estimated noise characteristics can be generalized to a longer time period is unclear and will only be verified by analyses of longer time series. Even then, extrapolating from one continuous site to another may not be valid because of possibly different local conditions. Nevertheless, recognizing these potential limitations, we compare in Table 6 typical annual campaign measurements of 5 consecutive days per site; semiannual measurements of 5 consecutive days per site; single-day monthly measurements; single-day weekly measurements; and daily (continuous) measurements. Velocity (1σ) uncertainties are estimated for different magnitudes of random walk noise (b_2) and flicker noise (b_1), assuming that in all cases the magnitude of white noise is $a = 2$ mm. In addition to the WN+FN and WN+RWN models, we look at the special cases of WN, FN, and RWN to quantify the individual contribution of each type of error.
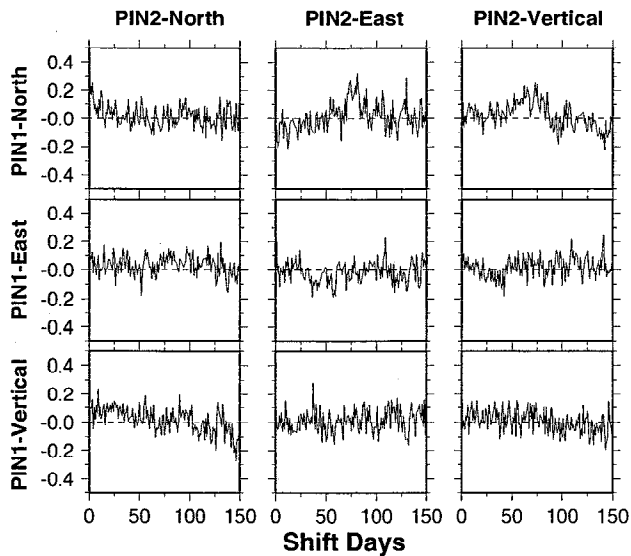
Figure 5. Weighted autocovariance functions of daily position time series of sites PIN1 and PIN2, in north, east, and vertical components for a time lag up to 150 days. The vertical scale denotes (unitless) covariances within the range [-0.5, 0.5].

In the case WN, we can achieve nearly an order of magnitude improvement in velocity uncertainty (1-σ) for continuous measurements (0.03 mm/yr) (see also Figure 7) compared to annual measurements (0.21 mm/yr). In the "best" case, FN will add $(0.07)^2$ mm^2 to the velocity variance, while RWN will add $(0.22)^2$ mm^2/yr^2 for all measurement scenarios. FN will only degrade velocity uncertainty significantly for continuous measurements and then by nearly a factor of 3 compared to WN. RWN will degrade velocity uncertainty by nearly a factor of 3 even for weekly measurements and nearly a factor of 8 for continuous measurements compared to WN. In the "typical" case, FN will degrade velocity uncertainty for annual to weekly measurements by a factor of 1.5–3.5, and by an order of magnitude for continuous measurements compared to WN. RWN will degrade velocity uncertainty for annual to weekly measurements by a factor of 4.5–10 and by a factor of 30 for continuous measurements compared to WN. Furthermore, there is little improvement achieved in observing continuously compared to observing annually. For the FN model velocity uncertainty is 0.3 mm/yr after 5 years of measurements and 3 times larger for RWN. In the "worst" case, velocity uncertainty is 0.7 mm/yr for FN and 2.2 mm/yr for RWN for all tested measurement scenarios.

Campaign GPS measurements are more prone to site survey errors than permanent GPS installations since the GPS antenna is almost always realigned over the geodetic mark (monument) for each measurement period. Careful field surveys, however, can minimize these errors, as demonstrated, for example, by *Genrich and Bock* [1992]. Other site-specific errors such as multipath, signal scattering, and antenna phase center variations may be more important for campaign surveys if the observation times are less than 24 hours. Continuous measurements allow for a degree of reduction in these types of errors since they tend to repeat on successive days [e.g., *Genrich and Bock*, 1992]. Finally, monumentation for campaign measurements is often less stable than for continuous measurements, with increased spatial density (i.e., more sites) thought to compensate for decreased site stability (this is the argument often made for installing large

continuous GPS networks with less expensive monuments). The comparisons in Table 6 assume that monumentation is of the same quality for both continuous and campaign measurements and that there are no site setup errors for the latter. Though not impossible to achieve, this is not the "typical" case. Nevertheless, under these assumptions, it is clear that random-walk-like motions exhibited by other types of continuous geodetic measurements [e.g., *Langbein and Johnson*, 1997], of order 1–1.5 mm/yr$^{0.5}$ even for well-anchored monuments, would limit the utility of continuous GPS measurements for estimation of interseismic deformation compared to infrequent but carefully surveyed campaign measurements. On the other hand, if continuous GPS position time series are fractal white noise processes with spectral indices of about 0.4 and the magnitude of colored noise can be kept at a reasonable level (~0.5–1.0 mm), then there is about a factor of 3 improvement in site velocity uncertainties achievable by continuous GPS measurements compared to less frequent measurements. However, if colored noise is of magnitude 2 mm or larger, there is no significant improvement when observing continuously. Reducing the magnitude of low-frequency colored noise is critical and is best accomplished by building sites with bedrock-anchored or deeply anchored monuments, whether these sites will be observed continuously or less frequently.

The choice of whether to use continuous GPS or field GPS measurements to monitor interseismic deformation becomes (1) a question of cost, a trade off between increased spatial resolution (e.g., building a larger number of stable monuments with only a subset surveyed by dedicated roving field crews) and installing unattended continuous sites, (2) a function of the desired velocity uncertainty, and (3) a function of the expected type and magnitude of colored noise in geodetic time series. More conclusive results on the latter will be obtained by analyzing longer spans of data and from arrays with a larger number of sites. Multimodal measurements that mix the two approaches as advocated by *Bevis et al.* [1997] may offer an alternative option for achieving a balance of enhanced spatial and temporal resolution.

Station Design

Our time series are not long enough to demonstrate the existence of random walk noise of order 1.5 mm/yr$^{0.5}$ reported by other investigators for longer continuous geodetic time series and attributed to motions of geodetic monuments. However, we cannot rule out random walk processes since much longer continuous time series from laser strain meters and two-color laser distance measurements do exhibit spectra that rise approximately as f^2. Furthermore, both of these measurement techniques are more precise than GPS, allowing a more accurate estimation of the random walk component. Terrestrial geodetic measurement techniques are much simpler in concept than space-based measurements and have a shorter list of possible measurement errors; the main similarity between the techniques is the need to firmly anchor the measurements to the subsurface.

Although the 19-month PGGA time series between the Landers and Northridge earthquakes is limited in duration, our analysis does provide some insight for continuous GPS station design. Table 1 summarizes the type of geodetic monument and gives a description of what equipment and other changes occurred at each site. We bin and score the ratio of FN and WN coefficients (b_1/a_1) for the WN+FN model which range between 0.5 and 1.7 for each time series as follows: [0.5–0.8] scores +1,
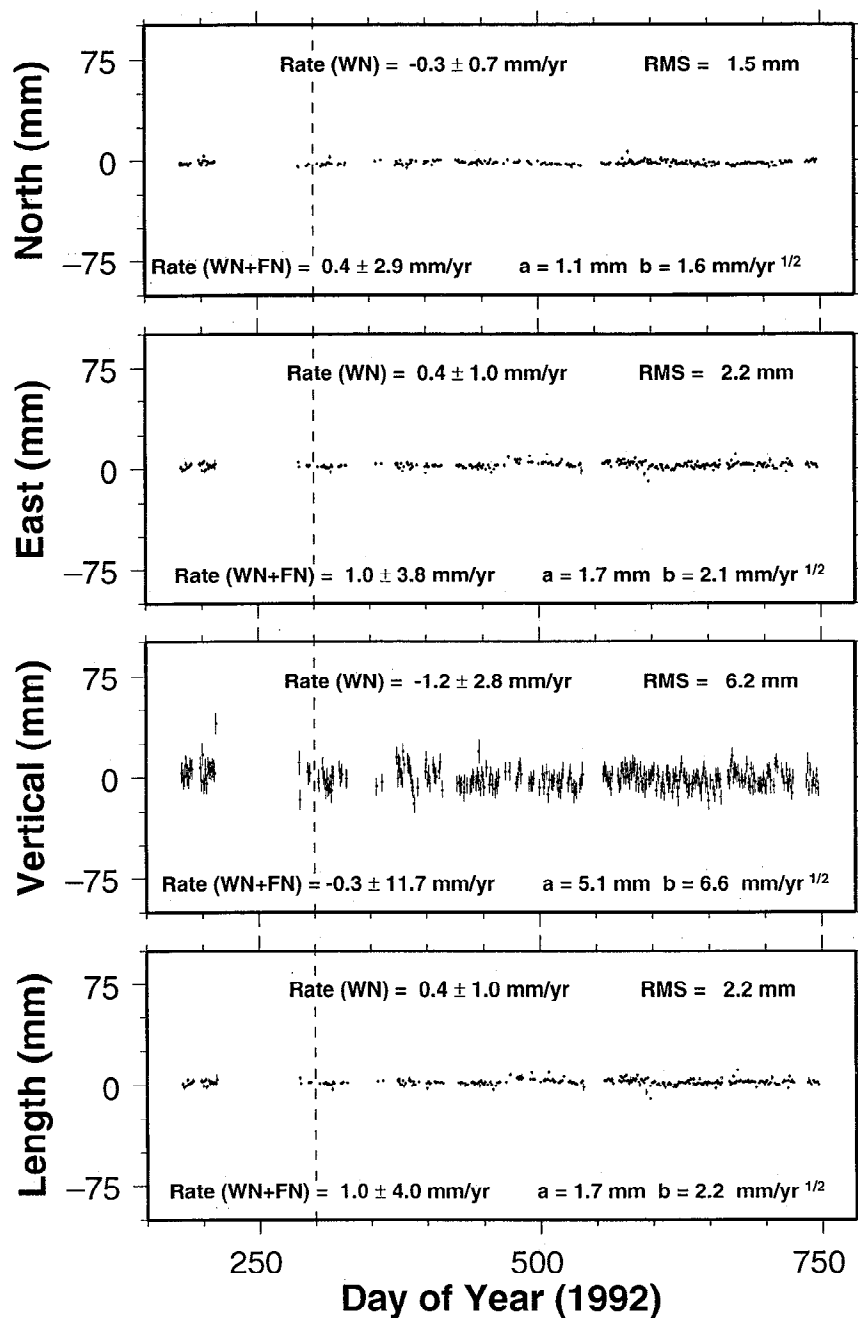
Figure 6. Relative component (baseline) time series for sites PIN1 and PIN2. The data to the left of the dashed vertical line are neglected in the estimation of the linear rate of displacement. Rate estimates and uncertainties are indicated for white noise (WN) and white noise plus flicker noise (WN+FN) models. The weighted RMS scatter for each component is shown in the upper right-hand corner of each panel. The scaling coefficients a and b for white noise and flicker noise coefficients, respectively, are indicated in the lower right-hand corner.

[0.9–1.2] scores 0, [1.3–1.7] scores -1. For example, MATH scores +3, JPLM scores -2. These are the highest and lowest scores, per site, respectively.

For sites with well-anchored monuments (bedrock or deeply anchored, see Table 1) the total score is +7; for sites with shallow anchoring and/or stability problems (JPLM, PVEP) or unconventional monumentation (GOLD, HARV), the total score is -3. If we exclude the vertical components which have larger white noise components, the total score is +3 for "good" monumentation; -3, otherwise. As in the autocorrelation analysis, the north component of GOLD and the east component of PVEP stand out as anomalous. From this we infer that the

time series with the least colored noise are those that have stable monumentation, whether deeply anchored with antennas more than 1.5 m above the surface (PIN1, PIN2, SIO3, VNDP) or anchored to bedrock with antennas about 0.2 m above the rock surface (MATH, ROCH). PGGA sites with questionable stability and marginal anchoring display larger flicker noise magnitudes in their time series.

For sites with no hardware changes, the total score is +2; for sites with hardware changes (and corrected antenna offsets), the score is the same; i.e., there is no apparent correlation between the ratio of FN and WN coefficients and these changes. Nevertheless, changes in equipment during the lifetime of an

Table 5. Pacific Plate Horizontal Velocity Estimates

Site Code	Component	FWN	WN+FN
Group 1			
GOLD	North	-29.0 ± 1.0	-28.6 ± 5.5
	East	21.0 ± 1.5	21.1 ± 5.6
JPLM	North	-7.9 ± 0.6	-7.6 ± 3.6
	East	2.4 ± 1.0	2.1 ± 6.1
SIO3	North	0.7 ± 0.6	0.7 ± 2.1
	East	4.5 ± 1.1	4.8 ± 4.0
VNDP	North	-1.3 ± 0.9	-1.0 ± 4.6
	East	1.6 ± 1.6	1.2 ± 6.6
Group 2			
PIN1	North	-10.8 ± 0.8	-10.1 ± 3.8
	East	18.2 ± 1.5	18.5 ± 5.5
PIN2	North	-10.5 ± 0.8	-10.7 ± 3.1
	East	17.8 ± 1.6	17.2 ± 4.1
ROCH	North	-6.5 ± 0.7	-6.5 ± 2.5
	East	14.0 ± 1.6	13.7 ± 7.3
Group 3			
HARV	North	-4.6 ± 2.0	-4.2 ± 9.2
	East	-0.8 ± 4.3	1.5 + 11.3
MATH	North	-4.9 ± 1.1	-4.8 ± 2.3
	East	7.6 ± 2.0	7.4 ± 5.3
PVEP	North	1.5 ± 1.8	0.5 ± 5.7
	East	-10.8 ± 3.5	-11.3 ± 15.2

Velocity estimates in millimeters per year for fractal white noise (FWN) and white noise plus flicker noise (WN+FN) models. See Figure 3. Uncertainties are 95% confidence intervals. Site groupings are explained in Table 1.

experiment, in particular antennas, will tend to reduce the detectability of geophysical signals. For example, in the estimation of site velocity (and measurement noise coefficients) with the MLE technique, a new offset parameter will generally need to be added for each antenna change. Thus it is good practice to avoid these changes if at all possible. The negative impact of these types of changes on continuous GPS time series may be reduced in the future by expected improvements in site and antenna calibrations.

Local site stability is essential, as it is for all types of precise geodetic measurements. Site PVEP (group 3, Table 1) is an example of a site with stable monumentation but is suspected of being locally unstable. Periodic surveys to nearby stable reference marks is good practice. A better but more expensive practice is to install stable continuous GPS sites in pairs at nearby marks (e.g., PIN1 and PIN2) to allow for the proper assessment of geodetic precision and enhanced detectability of geophysical signals.

Conclusions

We have analyzed the stochastic properties of continuous GPS position time series for the 19-month period between the 1992 Landers and 1994 Northridge earthquakes in southern California and determined that there is significant temporal correlation in all series, which is not reflected in the weighted RMS. Hence it is clear that this statistic, which is sometimes used to describe the repeatability or scatter of GPS position estimates, is unsuitable for describing long-term precision. We have tested colored noise
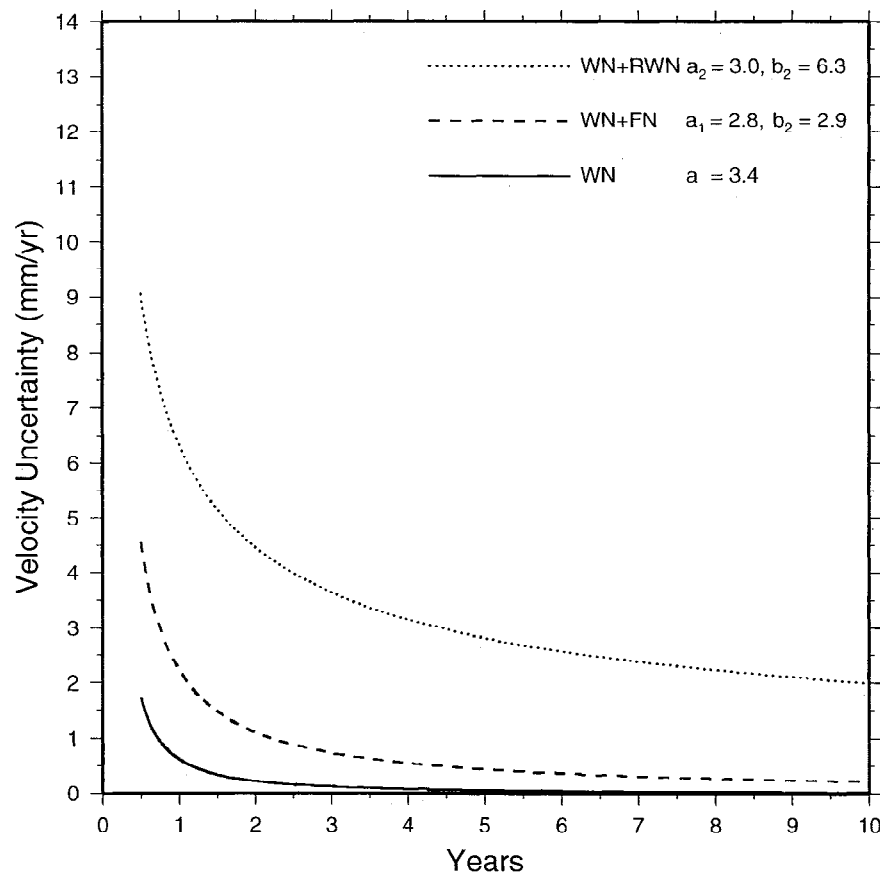

Figure 7. Velocity uncertainties for 0.5 to 10 years of continuous GPS measurements for three cases: white noise, WN (a = 3.4 mm); white noise plus flicker noise, WN+FN (a_1 = 2.8 mm, b_1 = 2.9 mm); and white noise plus random walk noise, WN+RWN (a_2 = 3.0 mm, b_2 = 6.3 mm/yr$^{0.5}$). The values for a, a_1, a_2, b_1, and b_2 are averages of the horizontal component scale factors given in Table 4.

Table 6. Site Velocity Uncertainties Extrapolated to a Five-Year Period

| Observations | | White Noise $a = 2$ $b = 0$ | Colored Noise $a = 0$ | | Mixed Noise "Best" Case, $a = 2$ | | Mixed Noise "Typical" Case, $a = 2$ | | Mixed Noise "Worst" Case, $a = 2$ | |
| | | | $b_1 = 0.5$ | $b_2 = 0.5$ | $b_1 = 0.5$ | $b_2 = 0.5$ | $b_1 = 2$ | $b_2 = 2$ | $b_1 = 5$ | $b_2 = 5$ |
Frequency	Number	WN	FN	RWN	WN+FN	WN+RWN	WN+FN	WN+RWN	WN+FN	WN+RWN
Annual	6	0.21	0.06	0.22	0.22	0.31	0.33	0.93	0.65	2.25
Semi-Annual	11	0.17	0.06	0.22	0.18	0.29	0.32	0.92	0.69	2.25
Monthly	61	0.17	0.07*	0.22	0.19	0.30	0.35	0.94	0.75	2.27
Weekly	261	0.09	0.07*	0.22	0.11	0.25	0.31	0.92	0.74	2.26
Daily	1826	0.03	0.07*	0.22	0.08	0.23	0.30	0.90	0.74	2.24

Site velocity uncertainties (1σ) achievable by five measurement scenarios, for the case of white noise (WN), flicker noise (FN), random walk noise (RWN), white noise plus flicker noise (WN+FN), and white noise plus random walk noise (WN+RWN). Scenarios tested include annual and semi-annual measurements of 5 consecutive days each, monthly and weekly measurements of 1 day each, and daily (continuous) measurements. Coefficients are a for WN (mm), b_1 for FN (mm), and b_2 for RWN (mm/yr$^{0.5}$). Units are millimeters per year for site velocities.

*The apparent slight increase in velocity uncertainty is due to the estimator being statistically inconsistent in the presence of flicker noise.

models with both integer and fractional spectral indices. For models with integer spectral indices, we assume that measurement error is a linear combination of a white noise process and either a flicker noise or random walk noise process and estimate by a maximum likelihood algorithm scaling coefficients for each process simultaneously with a linear rate of displacement. A white noise plus flicker noise model clearly fits the data better than a white noise model. However, we cannot distinguish between this two-component model and a single-component fractal white noise model. We estimate a spectral index of about 0.4 ± 0.2 (95% confidence interval) for the latter model. For the fractal white noise model, velocity uncertainties are 2–4 times larger than uncertainties derived from a white noise model; for the white noise plus flicker noise model, the velocity uncertainties are 3–6 times larger than the white noise model. The relatively short length of the time series, however, precludes a definitive rejection of the random walk noise processes seen in longer continuous geodetic data sets.

Time series of monuments anchored in bedrock or deeply anchored with surface-isolated, braced steel rods tend to reduce colored noise in the daily position estimates. Although sometimes expensive, sites that are not properly monumented may nullify improvements in velocity uncertainties achievable from continuous GPS measurements, compared to infrequent field measurements. Proper site selection is also critical in keeping position errors to a reasonable level.

Appendix A: Weighted Linear Regression With Equally Spaced Data

The linear regression problem can be expressed as fitting a straight line through a series of N points x_i taken at times t_i. The parameters that define the line are its x-intercept x_0 and slope r such that

$$x(t_i) = x_0 + rt_i + \varepsilon_x(t) \tag{A1}$$

We assume that the error term $\varepsilon_x(t)$ is a linear combination of a sequence of independent unit-variance random variables α_j and a sequence of temporally correlated random variables β_j such that

$$\varepsilon_x(t) = a\alpha_j(t) + b\beta_j(t) \tag{A2}$$

Scaling coefficients a and b are the magnitude of uncorrelated random error (white noise) and temporally correlated random

error (colored noise), respectively. We assume here that the temporal correlation is described by a random walk process. We can then express the covariance matrix of the measurements x_i as

$$C_x(t) = a^2\mathbf{I} + b^2\mathbf{J}_2(t) \tag{A3}$$

where $\mathbf{I}$ is the identity matrix of dimension N and $\mathbf{J}_2$ is the random walk covariance matrix such that (see equation (B3))

$$\mathbf{J}_2(t) = f_s^{-1}\begin{bmatrix} 1 & 1 & 1 & \cdots & 1 \\ 1 & 2 & 2 & \cdots & 2 \\ 1 & 2 & 3 & \cdots & 3 \\ \vdots & \vdots & \vdots & \ddots & \vdots \\ 1 & 2 & 3 & \cdots & N \end{bmatrix}; \; f_s = \frac{N-1}{T} \tag{A4}$$

where f_s is the sampling period in yr^{-1}, T is the total observation span, and N is the number of measurements [Johnson and Wyatt, 1994]. Fitting a straight line to the time series, i.e.,

$$\hat{x}(t_i) = \hat{x}_0 + \hat{r}t_i \tag{A5}$$

by weighted linear regression (least squares) yields estimates for x_0 and r

$$\hat{y} = [A^TC_x^{-1}A]^{-1}A^TC_x^{-1}x \tag{A6}$$

with covariance matrix (within a scale factor)

$$\hat{C}_{\hat{y}} = [A^TC_x^{-1}A]^{-1} \tag{A7}$$

where

$$x = (x_1, \cdots, x_N)^T \tag{A8}$$

$$A = \begin{bmatrix} 1 & t_1 \\ 1 & t_2 \\ \vdots & \vdots \\ 1 & t_N \end{bmatrix} \tag{A9}$$

$$y = (x_0, r)^T \tag{A10}$$

Uncorrelated Errors (White Noise)

In the case of uncorrelated errors only, $b=0$, it is easily shown that

$$\hat{C}_y^{-1} = a^{-2} \begin{bmatrix} N & \sum\limits_{i=1}^{N} t_i \\ \sum\limits_{i=1}^{N} t_i & \sum\limits_{i=1}^{N} t_i^2 \end{bmatrix} \qquad (A11)$$

and

$$\hat{C}_y = \begin{bmatrix} \sigma_{x_0}^2 & \sigma_{x_0 r} \\ \sigma_{x_0 r} & \sigma_r^2 \end{bmatrix} = a^2 \frac{\begin{bmatrix} \sum\limits_{i=1}^{N} t_i^2 & -\sum\limits_{i=1}^{N} t_i \\ -\sum\limits_{i=1}^{N} t_i & N \end{bmatrix}}{N \sum\limits_{i=1}^{N} t_i^2 - \left[\sum\limits_{i=1}^{N} t_i \right]^2} \qquad (A12)$$

The variance of the estimated x intercept for uncorrelated measurement errors (white noise) is then

$$\left(\sigma_{\hat{x}_0}^2 \right)_{WN} = a^2 \frac{\sum\limits_{i=1}^{N} t_i^2}{N \sum\limits_{i=1}^{N} t_i^2 - \left[\sum\limits_{i=1}^{N} t_i \right]^2} \qquad (A13)$$

and the variance of the estimated slope is

$$\left(\sigma_{\hat{r}}^2 \right)_{WN} = \frac{N a^2}{N \sum\limits_{i=1}^{N} t_i^2 - \left[\sum\limits_{i=1}^{N} t_i \right]^2} \qquad (A14)$$

These are well known formulas for the linear regression problem under the assumption of uncorrelated measurement error.

We now derive simpler expressions for (A13) and (A14) in the case of equally spaced data such that

$$t_i = (i-1)\Delta T; \quad T = (N-1)\Delta T \qquad (A15)$$

where ΔT is the sampling interval, and T is the total observation span. From (A14) and (A15)

$$\left(\sigma_{\hat{r}}^2 \right)_{WN} = \frac{N a^2}{N \Delta T^2 \sum\limits_{i=1}^{N} (i-1)^2 - \Delta T^2 \left[\sum\limits_{i=1}^{N} (i-1) \right]^2} \qquad (A16)$$

$$\left(\sigma_{\hat{r}}^2 \right)_{WN} = \frac{N a^2}{\Delta T^2 \left\{ N \sum\limits_{i=0}^{N-1} i^2 - \left(\sum\limits_{i=0}^{N-1} i \right)^2 \right\}} \qquad (A17)$$

Using the identities

$$\sum\limits_{i=1}^{n} k = \frac{n(n+1)}{2}; \quad \sum\limits_{i=1}^{n} k^2 = \frac{n(n+1)(2n+1)}{6} \qquad (A18)$$

we can express (A17) as

$$\left(\sigma_{\hat{r}}^2 \right)_{WN} = \frac{N a^2}{\Delta T^2 \left\{ \frac{N^2(N-1)(2N-1)}{6} - \left(\frac{N(N-1)}{2} \right)^2 \right\}} \qquad (A19)$$

which reduces to

$$\left(\sigma_{\hat{r}}^2 \right)_{WN} = \frac{a^2}{\Delta T^2} \frac{12}{N(N-1)(N+1)}; \quad N \geq 2 \qquad (A20)$$

or, using (A15),

$$\left(\sigma_{\hat{r}}^2 \right)_{WN} = \frac{a^2}{T^2} \frac{12(N-1)}{N(N+1)}; \quad N \geq 2 \qquad (A21)$$

Similarly, we can derive an expression for the x intercept variance

$$\left(\sigma_{\hat{x}_0}^2 \right)_{WN} = \frac{2a^2(2N-1)}{N(N+1)} \qquad (A22)$$

which is a function of the measurement error a and the number of measurements T. For large N, we see that

$$\left(\sigma_{\hat{r}}^2 \right)_{WN} \cong \frac{12a^2}{NT^2} \qquad (A23)$$

and

$$\left(\sigma_{\hat{x}_0}^2 \right)_{WN} \cong \frac{4a^2}{N} \qquad (A24)$$

Random Walk Errors

In the presence of only random walk errors, i.e., $a=0$, the inverse of the position covariance matrix (A3) is given by the tridiagonal matrix

$$J_2^{-1} = \frac{N-1}{T} \begin{bmatrix} 2 & -1 & 0 & 0 & \cdots & 0 \\ -1 & 2 & -1 & 0 & \cdots & 0 \\ 0 & -1 & 2 & \ddots & \ddots & \vdots \\ 0 & 0 & \ddots & \ddots & \ddots & 0 \\ \vdots & \vdots & \ddots & \ddots & 2 & -1 \\ 0 & 0 & \cdots & 0 & -1 & 1 \end{bmatrix} \qquad (A25)$$

and

$$\hat{C}_{\hat{y}}^{-1} = (A^T J_2^{-1} A)$$
$$= b^{-2} \frac{N-1}{T} \begin{bmatrix} 1 & t_1 \\ t_1 & C_{22} \end{bmatrix} \qquad (A26)$$

where

$$C_{22} = t_N^2 + 2 \sum\limits_{i=1}^{N-1} t_i^2 - 2 \sum\limits_{i=1}^{N-1} (t_i t_{i+1})$$

Using (A15) and (A18), C_{22} can be simplified to

$$\begin{aligned} C_{22} &= \Delta T^2 [(N-1)^2 + 2 \sum\limits_{i=1}^{N-1} (i-1)^2 - 2 \sum\limits_{i=1}^{N-1} (i)(i-1)] \\ &= \Delta T^2 [(N-1)^2 - 2 \sum\limits_{i=1}^{N-1} i + 2 \sum\limits_{i=1}^{N-1} 1] \\ &= \Delta T^2 [(N-1)^2 - N(N-1) + 2(N-1)] \\ &= (N-1) \Delta T^2 \end{aligned} \qquad (A27)$$

and hence

$$\begin{aligned} \hat{C}_{\hat{y}}^{-1} &= b^{-2} \frac{N-1}{T} \begin{bmatrix} 1 & 0 \\ 0 & (N-1)\Delta T^2 \end{bmatrix} \\ &= b^{-2} \begin{bmatrix} \frac{1}{\Delta T} & 0 \\ 0 & (N-1)\Delta T \end{bmatrix} \end{aligned} \qquad (A28)$$

Inverting (A28) yields

$$\hat{C}_{\hat{y}} = \frac{b^2}{N-1} \begin{bmatrix} (N-1)\Delta T & 0 \\ 0 & \frac{1}{\Delta T} \end{bmatrix} \qquad (A29)$$

so that

$$\left(\sigma_{\dot{r}}^2\right)_{RWN} = \frac{b^2}{(N-1)\,\Delta T} = \frac{b^2}{T}\,; N \geq 2 \tag{A30}$$

$$\left(\sigma_{\dot{x}_0}^2\right)_{RWN} = b^2 \Delta T = \frac{b^2 T}{(N-1)}\,; N \geq 2 \tag{A31}$$

$$\left(\sigma_{\dot{x}_0 \dot{r}}\right)_{RWN} = 0 \tag{A32}$$

Appendix B: Covariance Matrices for Integer Spectral Models

The covariance matrices for the three underlying integer spectral models, white noise (WN), random walk noise (RWN), and flicker noise (FN), are given in this appendix in order of increasing complexity.

White noise ($\kappa=0$). In this case, $b_\kappa = 0$, and

$$C_x = a^2 I \tag{B1}$$

That is, the covariance matrix is diagonal and independent of time.

Random walk noise ($\kappa=2$). In this case, $a=0$, and

$$C_x(t) = J_2(t) = f_s^{-1} \begin{bmatrix} 1 & 1 & 1 & \cdots & 1 \\ 1 & 2 & 2 & \cdots & 2 \\ 1 & 2 & 3 & \cdots & 3 \\ \vdots & \vdots & \vdots & \ddots & \vdots \\ 1 & 2 & 3 & \cdots & N \end{bmatrix}; f_s = \frac{N-1}{T} \tag{B2}$$

where f_s is the sampling frequency in yr^{-1}, T is the total observation span, and N is the number of measurements [Johnson and Wyatt, 1994]. Note that (B2) is for data that are equally spaced in time; for non-equally spaced data the expression is considerably more complicated.

Flicker noise ($\kappa=1$). In this case, $a=0$, and

$$C_x = J_1 = \left[\left(\frac{3}{4}\right)^2 \frac{(24 I - J_0)}{12}\right]_{N \times N} \tag{B3}$$

where element (i, k) of the symmetric matrix J_0 is given by

$$J_0 = \begin{cases} 0 \; ; \; i = k \\ \frac{\log(k-i)}{\log 2} + 2 \; ; \; i < k \end{cases} \tag{B4}$$

For example, for a time series of 1000 points,

$$J_1 = \begin{bmatrix} 1.125 & 1.031 & 0.984 & 0.957 & \cdots & 0.564 \\ & 1.125 & 1.031 & 0.984 & \cdots & 0.564 \\ & & 1.125 & 1.031 & \cdots & 0.564 \\ & & & \ddots & \ddots & \vdots \\ & & & & 1.125 & 1.031 \\ \text{Sym} & & & & & 1.125 \end{bmatrix}_{1000 \times 1000}$$

The constants in (B3) have been chosen so that power spectra for random walk noise and flicker noise cross at a frequency of yr^{-1} when coefficients b_1 and b_2 are both unity. Equation (B3) contains no reference to time or sampling frequency as did (B2); flicker noise, being on the asymptotic boundary between stationary and nonstationary processes, displays several odd traits: this is just one example.

References

Agnew, D. C., The time domain behavior of power-law noises, Geophys. Res. Lett., 19, 333-336, 1992.

Argus, D. F., and R. G. Gordon, No-net-rotation model of current plate velocities incorporating plate rotation model NUVEL-1, Geophys. Res. Lett., 18, 2039-2042, 1991.

Bevis, M., Y. Bock, P. Fang, R. Reilinger, T. A. Herring, J. Stowell, and R. Smalley, Blending old and new approaches to regional GPS geodesy, Eos Trans. AGU, 78, 61, 1997.

Bock Y., et al., Detection of crustal deformation from the Landers earthquake sequence using continuous geodetic measurements, Nature, 361, 337-340, 1993.

Bock Y., et al., Southern California Permanent GPS Geodetic Array: Continuous measurements of crustal deformation between the 1992 Landers and 1994 Northridge earthquakes, J. Geophys. Res., this issue.

Boucher, C., Z. Altamimi, and L. Duhem, Results and analysis of the ITRF93, IERS Tech. Note 18, Int. Earth Rotation Serv., Obs. de Paris, 1994.

Counselman, C. C., III, and S. A. Gourevitch, Miniature interferometer terminals for Earth surveying: Ambiguity and multipath with Global Positioning System, IEEE Trans. Geosci. Remote Sens., GE-19, 244-252, 1981.

Davis, A., A. Marshak, W. Wiscombe, and R. Calahan, Multifractal characterizations of nonstationarity and intermittency in geophysical fields: Observed, retrieved or simulated, J. Geophys. Res., 99, 8055-8072, 1994.

DeMets, C., R. G. Gordon, D. Argus, and S. Stein, Current plate motions, Geophys. J. Int., 101, 425-478, 1990.

DeMets, C., R. G. Gordon, D. Argus, and S. Stein, Effects of recent revisions to the geomagnetic reversal time scale on estimates of current plate motions, Geophys. Res. Lett., 21, 2191-2194, 1994.

Dong, D., and Y. Bock, Global Positioning System network analysis with phase ambiguity resolution applied to crustal deformation studies in California, J. Geophys. Res., 94, 3949-3966, 1989.

Elósegui, P., J. L. Davis, R. T. K. Jaldehag, J. M. Johansson, A. E. Niell and I. I. Shapiro, Geodesy using the Global Positioning System: The effects of signal scattering on estimates of site position, J. Geophys. Res., 100, 9921-9934, 1995.

Feigl, K. L., et al., Space geodetic measurement of crustal deformation in central and southern California, 1984-1992, J. Geophys. Res., 98, 21,677-21,712, 1993.

Genrich, J. F., and Y. Bock, Rapid resolution of crustal motion at short ranges with the Global Positioning System, J. Geophys. Res., 97, 3261-3269, 1992.

Genrich, J. F., Y. Bock, R. McCaffrey, E. Calais, C. W. Stevens, and C. Subarya, Accretion of the southern Banda arc to the Australian plate margin determined by Global Positioning System measurements, Tectonics, 15, 288-295, 1996.

Georgiadou, Y., and A. Kleusberg, On carrier signal multipath effects in relative GPS positioning, Manuscr. Geod. 13, 172-179, 1988.

Jaldehag, R. T. K., J. M. Johansson, J. L. Davis, and P. Elósegui, Geodesy using the Swedish permanent GPS network: Effects of snow accumulation on estimates of site positions, Geophys. Res. Lett., 23, 1601-1604, 1996.

Johnson, H. O., and F. K. Wyatt, Geodetic network design for fault-mechanics studies, Manuscr. Geod., 19, 309-323, 1994.

Johnson, H. O., and D. C. Agnew, Monument motion and measurements of crustal velocities, Geophys. Res. Lett., 22, 2905-2908, 1995.

Karcz, I., L. J. Morreale, and F. Porebski, Assessment of benchmark credibility in the study of recent vertical crustal movements, *Tectonophysics*, *33*, T1-T6, 1976.

Kendall, M., and A. Stuart, *The Advanced Theory of Statistics, vol. 2, Inference and Relationship*, pp. 240-274, Charles Griffin, London, 1979.

King, N. E., J. L. Svarc, E. B. Fogleman, W. K. Gross, K. W. Clark, G. D. Hamilton, C. H. Stiffler, and J. M. Sutton, Continuous GPS observation across the Hayward fault, California, 1991-1994, *J. Geophys. Res.*, *100*, 20,271-20,284, 1995.

Kolmogorov, A. N., Local structure of turbulence in an incompressible fluid for very large Reynolds number, *Dokl. Akad. Nauk SSSR*, *30*, 299-303, 1941.

Langbein, J. O., and H. Johnson, Noise level of geodetic monuments, *Eos Trans. AGU*, *76*, F142, 1995.

Langbein J., and H. Johnson, Correlated errors in geodetic time series: Implications for time-dependent deformation, *J. Geophys. Res.*, *102*, 591-604, 1997.

Langbein, J. O., M. F. Linker, A. F. McGarr, and L. E. Slater, Precision of two-color geodimeter measurements: Results from 15 months of observations, *J. Geophys. Res.*, *92*, 11,644-11,656, 1987.

Langbein, J. O., R. O. Burford and L. E. Slater, Variations in fault slip and strain accumulation at Parkfield, California: Initial results using two-color Geodimeter measurements, 1984-1988, *J. Geophys. Res.*, *95*, 2533-2552, 1990.

Langbein, J. O., F. Wyatt, H. Johnson, D. Hamann, and P. Zimmer, Improved stability of a deeply anchored geodetic monument for deformation monitoring, *Geophys. Res. Lett.*, *22*, 3533-3536, 1995.

Mandlebrot, B., *The Fractal Geometry of Nature*, W. H. Freeman, New York, 1983.

Mandlebrot, B., and J. Van Ness, Fractional Brownian motions, fractional noises, and applications, *SIAM Rev.*, *10*, 422-439, 1968.

Papoulis, A., *Probability, Random Variables, and Stochastic Processes*, McGraw-Hill, New York, 1965.

Priestley, M. B., *Spectral Analysis and Time Series*, Academic, San Diego, Calif., 1981.

Savage, J. C., and J. L. Svarc, Postseismic deformation associated with the 1992 M_W=7.3 Landers earthquake, southern California, *J. Geophys. Res.*, *102*, 7565-7577, 1997.

Scargle, J. D., Studies in astronomical time series analysis, II, Statistical aspects of spectral analysis of unevenly spaced points, *Astrophys. J.*, *263*, 835-853, 1982.

Schupler, B. R., R. L. Allhouse, and T. A. Clark, Signal characteristics of GPS user antennas, *Navigation*, *41*, 277-295, 1994.

Wdowinski, S., Y. Bock, J. Zhang, P. Fang, and J. F. Genrich, Southern California Permanent GPS Geodetic Array: Spatial filtering of daily positions for estimating coseismic and postseismic displacements induced by the 1992 Landers earthquake, *J. Geophys. Res.*, this issue.

Wessel, P., and W. H. F. Smith, Free software helps map and display data, *Eos Trans. AGU*, *72*, 445-446, 1991.

Wyatt, F., Displacements of surface monuments: Horizontal motion, *J. Geophys. Res.*, *87*, 979-989, 1982.

Wyatt, F., Displacements of surface monuments: Vertical motion, *J. Geophys. Res.*, *94*, 1655-1664, 1989.

Wyatt F., K. Beckstrom, and J. Berger, The optical anchor—A geophysical strainmeter, *Bull. Seismol. Soc. Am.*, *72*, 1701-1715, 1982.

Wyatt, F. K., H. Bolton, S. Bralla, and D. C. Agnew, New designs of geodetic monuments for use with GPS, *Eos Trans. AGU*, *70*, 1054-1055, 1989.

J. Behr, Y. Bock, P. Fang, J. Genrich, H. Johnson, S. Williams, and J. Zhang, Cecil H. and Ida M. Green Institute of Geophysics and Planetary Physics, Scripps Institution of Oceanography, 9500 Gilman Drive, La Jolla, CA 92093. (email: behr@gps.caltech.edu; ybock@ucsd.edu; pfang@pgga.ucsd.edu; jeff@pgga.ucsd.edu; johnson@ramsden.ucsd.edu; simon@pgga.ucsd.edu; jie@illustra.com)

S. Wdowinski, Department of Geophysics and Planetary Physics, Tel Aviv University, Ramat Aviv, 69978, Israel. (shimon@geo1.tau.ac.il)